

RESEARCH ARTICLE SUMMARY

HUMAN DEVELOPMENT

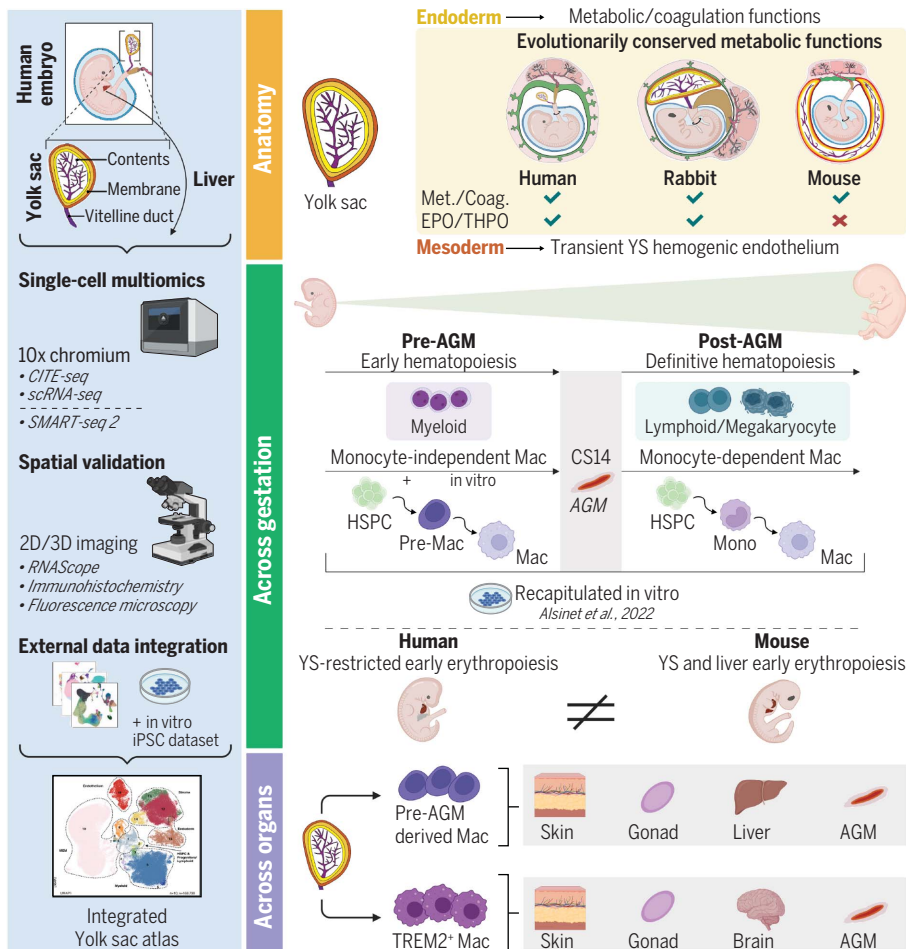
Yolk sac cell atlas reveals multiorgan functions during human early development

Issac Goh[†] and Rachel A. Botting[†] *et al.*

INTRODUCTION: The yolk sac (YS) generates the first blood and immune cells and provides nutritional and metabolic support to the developing embryo. Our current understanding of its functions derives from pivotal studies in model systems, and insights from human studies are limited. Single-cell genomics technologies have facilitated the interrogation of human developmental tissues at unprecedented resolution. Atlases of blood and immune cells from multiple organs have been

greatly enhanced by focused, time-resolved analyses of specific tissues.

RATIONALE: To characterize the functions of the human YS, we performed single-cell RNA sequencing (scRNA-seq) and cellular indexing of transcriptomes and epitopes by sequencing (CITE-seq) on the YS and paired embryonic liver. After integration with external datasets, our reference comprised 169,798 cells from 10 samples spanning 4 to 8 postconception weeks



Multiorgan functions of the human YS. We characterized functions of the developing human YS, combining scRNA-seq and CITE-seq with 2D and 3D imaging techniques. Our findings revealed YS contributions to metabolic and nutritional support and to early hematopoiesis. We characterized myeloid bias in early hematopoiesis, distinct myeloid differentiation trajectories, evolutionary divergence in initial erythropoiesis, and YS contributions to developing tissue macrophages. Met., metabolic; Coag., coagulation; Mac, macrophage. [Figure created with Biorender]

(PCW) or Carnegie stages (CS) 10 to 23. A repertoire of two-dimensional (2D) and 3D imaging techniques provided spatial context and validation. We compared the products of two hematopoietic inducible pluripotent stem cell (iPSC) culture protocols against our reference.

RESULTS: We determined that YS metabolic and nutritional support originates in the endoderm and that the endoderm produces coagulation proteins and hematopoietic growth factors [erythropoietin (EPO) and thrombopoietin (THPO)]. Although metabolic and coagulation protein production was conserved among humans, mice, and rabbits, EPO and THPO production was observed in humans and rabbits only.

We reconstructed trajectories from the YS hemogenic endothelium to early hematopoietic stem and progenitor cells (HSPCs). Using transcriptomic signatures of early and definitive hematopoiesis, we parsed YS HSPCs into myeloid-biased early HSPCs and lymphoid- and megakaryocyte-biased definitive HSPCs. Human embryonic liver remained macroscopically pale before CS14, when hematopoietic cells first emerge from the aorta-gonad-mesonephros (AGM) region. Tracking hemoglobin (Hb) subtypes led us to conclude that initial erythropoiesis is YS restricted. By contrast, in mice, Hb subtypes suggested two waves of pre-AGM erythropoiesis, including maturation in the macroscopically red embryonic liver.

Before CS14, monocytes were absent and macrophages originated from HPSCs via a pre-macrophage cell state. After CS14, monocytes emerged and a second, monocyte-dependent differentiation trajectory was reconstructed. A rare subset of *TREM2*⁺ macrophages, with a microglia-like transcriptomic signature, was present after CS14. The iPSC system optimized for macrophage production recapitulated the two routes to macrophage differentiation but did not generate the diversity of macrophages (including *TREM2*⁺ macrophages) observed in developing tissues.

CONCLUSION: Our study illuminates a previously obscure phase of human development, where vital functions are delivered by the YS acting as a transient extraembryonic organ. Our comprehensive single-cell atlas represents a valuable resource for studying the cellular differentiation pathways specific to early life and leveraging these for tissue engineering and cellular therapy. ■

The full author list and the list of author affiliations are available in the full article online.

*Corresponding authors: Laura Jardine (laura.jardine@ncl.ac.uk); Berthold Göttgens (bg200@cam.ac.uk); Sarah A. Teichmann (st9@sanger.ac.uk); Muzlifah Haniffa (mh32@sanger.ac.uk)

[†]These authors contributed equally to this work.

Cite this article as I. Goh *et al.*, *Science* **381**, eadd7564 (2023). DOI: 10.1126/science.add7564

READ THE FULL ARTICLE AT
<https://doi.org/10.1126/science.add7564>

RESEARCH ARTICLE

HUMAN DEVELOPMENT

Yolk sac cell atlas reveals multiorgan functions during human early development

Issac Goh^{1,2†}, Rachel A. Botting^{1,2†}, Antony Rose^{1,2†}, Simone Webb^{1,2†}, Justin Engelbert², Yorick Gitton³, Emily Stephenson^{1,2}, Mariana Quiroga Londoño⁴, Michael Mather², Nicole Mende⁴, Ivan Imaz-Rosshandler^{4,5}, Lu Yang¹, Dave Horsfall^{1,2}, Daniela Basurto-Lozada^{1,2}, Nana-Jane Chipampe¹, Victoria Rook¹, Jimmy Tsz Hang Lee¹, Mai-Linh Ton⁴, Daniel Keitley^{1,6}, Pavel Mazin¹, M. S. Vijayabaskar⁴, Rebecca Hannah⁴, Laure Gambardella¹, Kile Green⁷, Stephane Ballereau¹, Megumi Inoue³, Elizabeth Tuck¹, Valentina Lorenzi¹, Kwasi Kwakwa¹, Clara Alsinet^{1,8}, Bayanne Olabi^{1,2}, Mohi Miah^{1,2}, Chloe Admane^{1,2}, Dorin-Mirel Popescu², Meghan Acres², David Dixon², Thomas Ness⁹, Rowen Coulthard⁹, Steven Liso², Deborah J. Henderson², Emma Dann¹, Chenqu Suo¹, Sarah J. Kinston⁴, Jong-eun Park¹⁰, Krzysztof Polanski¹, John Marioni^{1,11,12}, Stijn van Dongen¹, Kerstin B. Meyer¹, Marella de Bruijn¹³, James Palis¹⁴, Sam Behjati^{1,15}, Elisa Laurenti⁴, Nicola K. Wilson⁴, Roser Vento-Tormo¹, Alain Chédotal³, Omer Bayraktar¹⁶, Irene Roberts¹⁶, Laura Jardine^{1,2*}, Berthold Göttgens^{4*}, Sarah A. Teichmann^{1,17*}, Muzlifah Haniffa^{1,2,18*}

The extraembryonic yolk sac (YS) ensures delivery of nutritional support and oxygen to the developing embryo but remains ill-defined in humans. We therefore assembled a comprehensive multiomic reference of the human YS from 3 to 8 postconception weeks by integrating single-cell protein and gene expression data. Beyond its recognized role as a site of hematopoiesis, we highlight roles in metabolism, coagulation, vascular development, and hematopoietic regulation. We reconstructed the emergence and decline of YS hematopoietic stem and progenitor cells from hemogenic endothelium and revealed a YS-specific accelerated route to macrophage production that seeds developing organs. The multiorgan functions of the YS are superseded as intraembryonic organs develop, effecting a multifaceted relay of vital functions as pregnancy proceeds.

The primary human yolk sac (YS) derives from the hypoblast at the time of embryo implantation [Carnegie stage 4 (CS4); ~1 postconception week (PCW)] (1, 2). The secondary YS supersedes the primary structure at around CS6 (~2.5 PCW) and persists until CS23 (~8 PCW) (1, 2). The secondary YS has three tissue compartments: the mesothelium (an epithelial layer interfacing the amniotic fluid), the mesoderm (including endothelial cells, blood cells, and smooth muscle), and the endoderm (an inner layer interfacing the vitelline fluid-filled YS cavity) (1). The functions of the YS in nutrient uptake, transport, and metabolism are phylogenetically conserved (2).

Hematopoiesis originates in the YS of mammals, birds, and some ray-finned fishes (3). The first wave of mouse YS hematopoiesis yields primitive erythroid cells, macrophages, and megakaryocytes (MKs) from embryonic day 7.5 (E7.5) (3, 4). After circulation begins, a second wave of erythromyeloid and lymphomylloid progenitors arise in the YS and supply the embryo (5). Finally, definitive hematopoietic stem cells arise in the aorta-gonad-mesonephros (AGM) region of the dorsal aorta and seed the fetal liver (6). Limited evidence suggests that the YS also provides the first blood cells during human development. Primitive erythroblasts ex-

pressing embryonic globin genes, surrounded by endothelium, emerge in the YS at CS6 (~2.5 PCW) (7, 8). Hematopoietic progenitors and macrophages are detectable at CS11 (~4 PCW) (9), with MKs, monocytes, mast cells, and innate lymphocytes also reported (9, 10). Long-term multilineage repopulating (definitive) hematopoietic stem and progenitor cells (HSPCs) originate in the AGM at CS14 (~5 PCW) (11). Equivalent cells are subsequently found in the YS at CS16 and the liver from CS17 (11, 12).

In this study, we report a time-resolved atlas of the human YS, combining single-cell protein and gene expression with imaging. This provides a comprehensive depiction of the metabolic and hematopoietic functions of the human YS as well as a benchmark for in vitro culture systems aiming to recapitulate human early development.

A single-cell atlas of human YS

We performed droplet-based single-cell RNA sequencing (scRNA-seq) to profile the human YS and integrated with external datasets to yield 169,798 high-quality cells from 10 samples spanning 4 to 8 PCW (CS10 to CS23), which can be interrogated on our interactive web portal [https://developmentalcellatlas.io/yolk-sac (13)] (Fig. 1, A to C; fig. S1, A to C; and data S1 to S18). Graph-based Leiden clustering yielded 39 cell types

grouped into 15 broad categories, including hematopoietic cells, endoderm, mesoderm, and mesothelium. Key marker genes were validated by plate-based scRNA-seq (Smart-seq2) (Fig. 1, C and D; fig. S1, B to F; and data S3 to S5, S8, S17, and S18). We used the term “HSPC” for cells collectively on the basis of their expression of a core HSPC signature (e.g., *CD34*, *SPINK2*, and *HLF*) without implying long-term repopulating capacity or multilineage potential. With comparison datasets, unless otherwise specified, we adopted published annotations (data S6 and S7). Surface protein expression from cellular indexing of transcriptomes and epitopes by sequencing (CITE-seq) of $n = 2$ YS cell suspensions (fig. S1, G and H) identified combinatorial antigens for cell purification and functional characterization (fig. S2A and data S9, S19, and S20). We generated matched embryonic liver scRNA-seq and CITE-seq data (fig. S2, B to F; fig. S3, A to C; and data S5, S10, S21, and S22), which confirmed the presence of discrete B cell progenitor stages only in the liver (fig. S3C and data S12). Around half of the YS lymphoid cells were innate lymphoid progenitors, which terminated in natural killer (NK) and innate lymphoid cell (ILC) precursor states on force-directed graph (FDG) visualization (fig. S3D). A small population of cells were referred to as “lymphoid B lineage” because of their expression of *CD19*, *CD79B*, and *IGLL1*. These cells did not express the typical B1 markers *CD5*, *CD27*, or *CCR10*, however. Given

¹Wellcome Sanger Institute, Wellcome Genome Campus, Hinxton, Cambridge CB10 1SA, UK. ²Biosciences Institute, Newcastle University, Newcastle upon Tyne NE2 4HH, UK.

³Sorbonne Université, INSERM, CNRS, Institut de la Vision, Paris, France. ⁴Department of Haematology, Wellcome-MRC Cambridge Stem Cell Institute, Cambridge CB2 0AW, UK.

⁵MRC Laboratory of Molecular Biology, Cambridge

Biomedical Campus, Cambridge CB2 0QH, UK. ⁶Department of Zoology, University of Cambridge, Cambridge CB2 3EJ, UK. ⁷Translational and Clinical Research Institute, Newcastle University, Newcastle upon Tyne NE2 4HH, UK. ⁸Centre

Nacional d'Anàlisi Genòmica-Centre de Regulació Genòmica (CNAG-CRG), Barcelona Institute of Science and Technology (BIST), Barcelona, Spain. ⁹NovoPath, Department of

Pathology, Newcastle Hospitals NHS Foundation Trust, Newcastle upon Tyne NE1 4LP, UK. ¹⁰Korea Advanced Institute of Science and Technology, Daejeon, South Korea.

¹¹EMBL-EBI, Wellcome Genome Campus, Cambridge CB10 1SD, UK. ¹²CRUK Cambridge Institute, University of

Cambridge, Cambridge CB2 0RE, UK. ¹³MRC Molecular Haematology Unit, MRC Weatherall Institute of Molecular

Medicine, Radcliffe Department of Medicine, University of Oxford, Oxford OX3 9DS, UK. ¹⁴Department of Pediatrics, University of Rochester Medical Center, Rochester, NY 14642, USA. ¹⁵Department of Paediatrics, University of Cambridge,

Cambridge CB2 0QQ, UK. ¹⁶Department of Paediatrics, University of Oxford, Oxford OX3 9DS, UK. ¹⁷Theory of Condensed Matter Group, Department of Physics, Cavendish

Laboratory, University of Cambridge, Cambridge CB3 0HE, UK. ¹⁸Department of Dermatology and NIHR Newcastle Biomedical Research Centre, Newcastle Hospitals NHS

Foundation Trust, Newcastle upon Tyne NE1 4LP, UK.

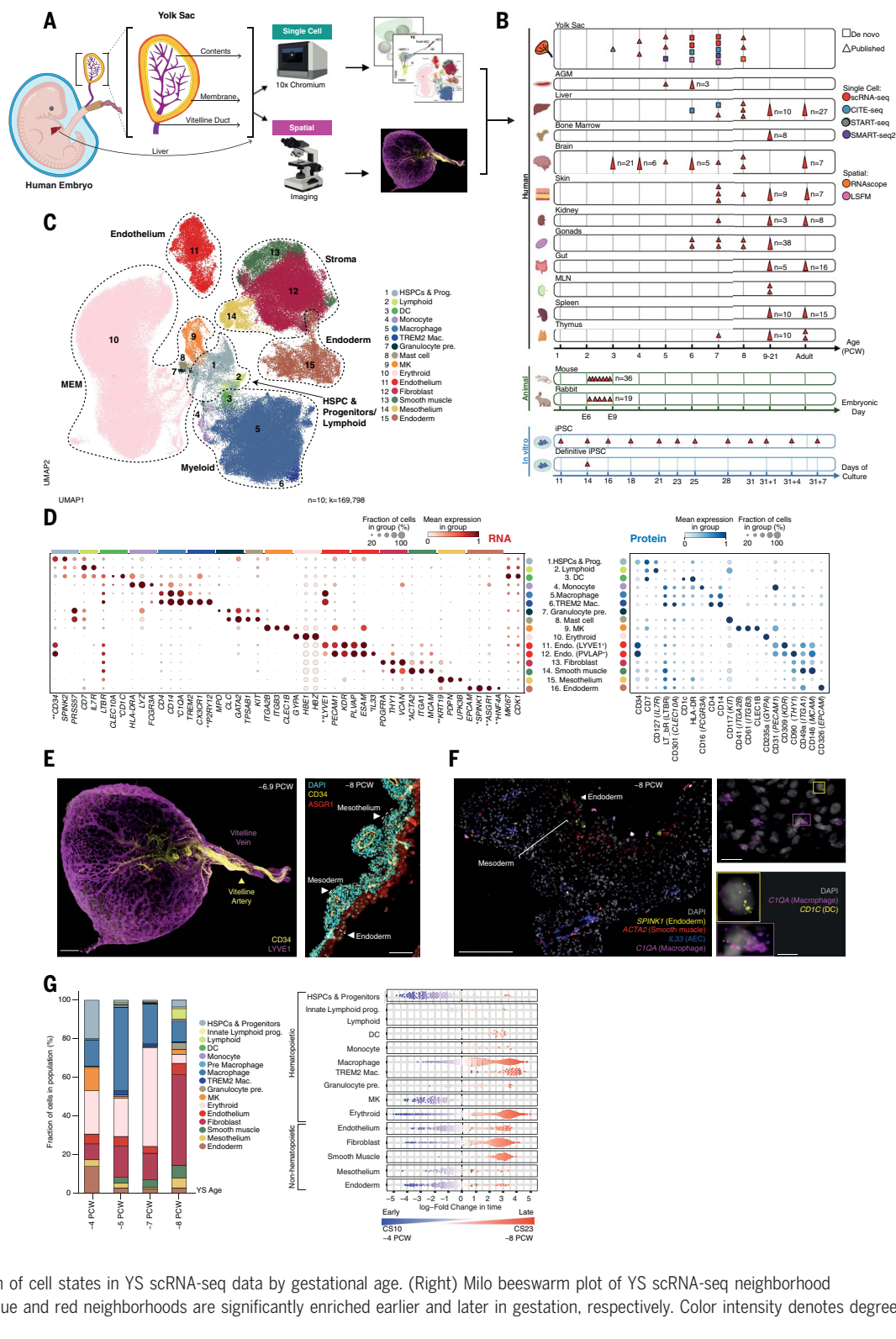
*Corresponding author. Email: laura.jardine@ncl.ac.uk (L.J.); bg200@cam.ac.uk (B.G.); st9@sanger.ac.uk (S.A.T.); mh32@sanger.ac.uk (M.H.)

†These authors contributed equally to this work.

‡These authors contributed equally to this work.

Fig. 1. A single-cell atlas of the human YS.

(A) Schematic of experimental outline. **(B)** Summary of data included in analyses. Squares represent new data, and triangles represent published data: YS (10, 12, 48, 63), AGM (12), liver (10), fetal BM (34), fetal brain (55), fetal skin (48), fetal kidney (74), fetal gonads (49), mouse (75), and iPSC (12, 20). Color indicates assay used (data S6). **(C)** UMAP visualization of YS scRNA-seq data ($n = 10$; $k = 169,798$). Colors represent broad cell states. Mac, macrophage; MEM, megakaryocyte-erythroid-mast cell lineage; pre., precursor; prog., progenitors. **(D)** (Left) Dot plot showing the mean expression (color) and proportion of cells expressing genes (dot size) of broad cell states in YS scRNA-seq data. (Right) Equivalent protein expression (color) and proportion of cells expressing proteins (dot size) from YS CITE-seq data ($n = 2$; $k = 3578$). Equivalent gene names are in parentheses. One asterisk indicates genes validated by RNA-seq, and two asterisks indicates proteins validated by IHC and/or immunofluorescence (IF) (data S4). Data are variance-scaled and min-max-standardized. **(E)** (Left) Light-sheet fluorescence microscopy of $CD34^+$ and $LYVE1^+$ vascular structures in YS (representative ~6.9 PCW sample). Scale bar, 500 μ m (movie S1). (Right) Immunofluorescence of an ~8-PCW YS highlighting endoderm (ASGR1; red) and endothelium (CD34; yellow) costained with DAPI (cyan). Scale bar, 100 μ m (data S23). **(F)** RNA-scope of YS (representative 8-PCW sample). (Left) Endoderm (*SPINK1*; yellow), smooth muscle (*ACTA2*; red), AEC (*IL33*; blue), and macrophages (*CIQA*; magenta). Scale bar, 200 μ m. (Right) DCs (*CD1C*; yellow box) and macrophages (*CIQA*; magenta box). Scale bar, 50 μ m. Individual channels are shown in fig. S4A. **(G)** (Left) Bar graph showing the proportion representation of cell states in YS scRNA-seq data by gestational age. (Right) Milo beeswarm plot of YS scRNA-seq neighborhood differential abundance across time. Blue and red neighborhoods are significantly enriched earlier and later in gestation, respectively. Color intensity denotes degree of significance (data S24).



the absence of distinct B cell progenitor stages and their later emergence (>5 PCW), these may constitute migratory B cells of fetal liver origin (fig. S3, D and E).

Three-dimensional visualization of the YS by light-sheet microscopy marked the $CD34^{\text{hi}}LYVE1^{\text{lo}}$

vitelline artery and $CD34^{\text{lo}}LYVE1^{\text{hi}}$ vitelline vein contiguous with a branching network of $CD34^{\text{lo}}LYVE1^{\text{hi}}$ vessels (Fig. 1E, fig. S3F, data S23, and movies S1 and S2). The $CD34^{\text{lo}}LYVE1^{\text{hi}}IL33^+$ vessels were situated within the mesoderm, a distinct layer beneath the $ASGR1^+SPINK1^+$

endoderm (Fig. 1, E and F; fig. S3, F to I; and fig. S4, A and B). $ACTA2^+$ smooth muscle cells formed a sublayer between the mesoderm and endoderm (Fig. 1F and fig. S4, A and B). Macrophages ($CIQA^+CD1C^{+/-}$) and a small number of dendritic cells (DCs) ($CIQA^{+/-}CD1C^+$) were

identified within the mesoderm (Fig. 1F and fig. S4A).

The most prevalent hematopoietic cell types in the early YS (CS10; ~4 PCW) were HSPCs, erythroid cells, macrophages, and MKs. Both HSPCs and MKs proportionately diminished thereafter, whereas erythroid cells and macrophages were sustained. DCs and *TREM2*⁺ macrophages did not emerge until >6 PCW (Fig. 1G and data S4). The ratio of hematopoietic to nonhematopoietic cells was around 3:1 in the early YS (CS10; ~4 PCW), with endoderm relatively abundant (Fig. 1G). The ratio approached 1:3 in the late YS (CS22 to CS23; ~8 PCW) because of the expansion of fibroblasts (Fig. 1G). The transcriptional profile of MKs was consistent across gestation, but both erythroid cells and macrophages had early and late gestation-specific molecular states, suggesting dual waves of production (Fig. 1G, fig. S4C, and data S24).

Multigorgan functions of YS

YS endoderm coexpressing *APOA1/2*, *APOC3*, and *TTR* (similar to embryonic or fetal hepatocytes), was present from gastrulation at ~2 to 3 PCW (14) (Fig. 2A and data S3, S7, and S21). The YS endoderm expressed higher levels of serine protease 3 (*PRSS3*), glutathione S-transferase alpha 2 (*GSTA2*), and multifunctional protein galectin 3 (*LGALS3*) compared with embryonic liver hepatocytes, whereas hepatocytes expressed a more extensive repertoire of detoxification enzymes, including alcohol and aldehyde dehydrogenases and cytochrome P450 enzymes (fig. S4D and data S3, S7, and S21). Both cell states shared gene modules implicated in coagulation and lipid and glucose metabolism (Fig. 2B and data S25), which were also conserved in mouse and rabbit extraembryonic endoderm (fig. S4, E and F, and data S25). The expression of transport proteins (alpha-fetoprotein and albumin), a protease inhibitor (alpha-1-antitrypsin), erythropoietin (EPO), and coagulation proteins (thrombin, prothrombin, and fibrin) were validated in human YS endoderm and embryonic liver hepatocytes (Fig. 2C and fig. S4G).

From the earliest time points, the YS endoderm expressed genes for anticoagulant proteins antithrombin III (*SERPINC1*) and protein S (*PROS1*) and components of the tissue factor-activated extrinsic coagulation pathway—thrombin (*F2*), factor VII (*F7*), and factor X (*F10*) (Fig. 2D and data S25), confirmed at the protein level for thrombin (Fig. 2C). Intrinsic pathway factors VIII, IX, XI, and XII (*F8*, *F9*, *F11*, and *F12*) were minimally expressed in the YS but were expressed by embryonic liver hepatocytes (Fig. 2D). Tissue factor, antithrombin III, and fibrinogen subunits were also expressed in mouse extraembryonic endoderm and rabbit YS endoderm (fig. S4E). Embryonic lethality of homozygous-null mice lacking prothrombin, thrombin, and coagulation factor V before liver synthetic func-

tion (i.e., at E9 to E12) implies functional relevance of YS expression (Fig. 2D and data S25) (15, 16), whereby coagulant and anticoagulant pathways develop in parallel to balance hemostasis.

YS endoderm cells expressed EPO and thrombopoietin (THPO) that are critical for erythropoiesis and megakaryopoiesis (Fig. 2, C and D; fig. S4H; and data S25 and S26). In mouse development, EPO is produced by the fetal liver and is only essential for definitive and the later stages of primitive erythropoiesis, with *Epo/Epor* knockout mice dying at around E13 (17). An EPO source before liver development is therefore likely not needed in mice. Accordingly, EPO has not been found in the mouse YS (18) (fig. S4E). In parallel to the human YS, rabbit YS endoderm also produced EPO at gestational stages preceding liver development (fig. S4E). We compiled a 12-organ integrated human fetal atlas spanning 3 to 19 PCW ($k = 3.12$ million cells, $n = 150$ donors; fig. S8, G and H, and data S6 and S7) and observed that EPO and THPO production were restricted to the YS and liver (fig. S4H), specifically to YS endoderm and liver hepatocytes (fig. S4I). Differentially expressed genes (DEGs) between the early and late YS endoderm revealed active retinoic acid and lipid metabolic processes until 7 PCW, after which genes associated with cell stress and death were expressed (Fig. 2E and data S26). A decline in the proportion of YS endoderm cells producing EPO was compensated by the onset of EPO production by hepatocytes at 7 PCW (fig. S4J). Thus, the human YS plays a critical role supporting hematopoiesis, metabolism, coagulation, and erythroid cell mass regulation before these functions are taken over by the embryonic or fetal liver and then, ultimately, by the adult liver (metabolism and coagulation), bone marrow (BM) (hematopoiesis), and kidney (erythroid cell mass regulation) (Fig. 2F).

Early versus definitive hematopoiesis in the YS and liver

Human YS hematopoietic progenitors spanned two groups: HSPCs characterized by *SPINK2*, *CYTLL1*, and *HOXB9* expression and cycling HSPCs characterized by cell cycle-associated genes, such as *MKI67* and *TOP2A* (fig. S5A and data S17). Using markers recently associated with early (*DDIT4*, *SLC2A3*, *RGS16*, and *LIN28A*) and definitive (*KIT*, *ITGA4*, *CD74*, and *PROCR*) HSPCs (12), we identified early and definitive fractions within both HSPCs and cycling HSPCs (Fig. 3, A to C). Early and definitive HSPCs expressed canonical HSPC genes, such as *SPINK2*, *HOPX*, and *HLF* (Fig. 3A and data S17), but diverged in expression of genes involved in multiple processes, such as enzymes (*GADI*), growth factors (*FGF23*), adhesion molecules (*SELL*), and patterning genes (*HOXA7*) (fig. S5C and data S17). By logistic regression (LR), YS HSPCs had a high median probability of class corre-

spondence to liver hematopoietic stem cells (HSCs), but this probability was higher for definitive than for early HSPCs (fig. S5B). YS cycling HSPCs had a bipartite probability distribution between liver multipotential progenitor (MPP) and common myeloid progenitor (CMP), with the definitive cycling HSPC more MPP-like compared with the early version. Differential protein expression in YS CITE-seq data indicated that CD122, CD194 (CCR4), and CD357 mark early HSPCs, whereas CD44, CD48, CD93, and CD197 (CCR7) mark definitive HSPCs (fig. S5D and data S27), in keeping with the reported use of CD34 and CD44 to segregate early- and definitive-type HSPCs by fluorescence-activated cell sorting (FACS) (19). We confirmed that an induced pluripotent stem cell (iPSC)-derived culture system reported to generate definitive HSPCs did express RNA markers characteristic of definitive HSPCs (12), but an iPSC-derived culture system optimized for macrophage production (20) did not (Fig. 3A).

To assess cross-tissue HSPC heterogeneity, we integrated HSPCs across hematopoietic organs (Fig. 3C, fig. S5E, and data S6 and S7). By kernel density estimation (KDE) score on integrated uniform manifold approximation (UMAP) embeddings, YS definitive HSPCs qualitatively colocalized with definitive HSPCs from age-matched liver (Fig. 3C and fig. S5E). From exclusively early HSPCs at ~3 PCW, we observed rapid accumulation of definitive HSPCs after AGM development CS14 (~5 PCW), likely accounting for the increase in the YS HSPC/progenitor fraction at 8 PCW (Fig. 1G, Fig. 3B, and fig. S5F).

Next, we examined the transition from YS to liver hematopoiesis. Before AGM, the human embryonic liver is macroscopically pale, which suggests that erythropoiesis predominantly occurs in the YS (Fig. 3D). We tracked the proportional representation of hemoglobin (Hb) subtypes over time as a proxy for YS versus embryonic liver contributions. *HBZ* and *HBE1* (genes for Hb Gower 1) were restricted to YS erythroblasts, whereas *HBG1* (which forms fetal Hb/HbF in combination with an alpha chain) was expressed in fetal liver erythroblasts (21–25) (Fig. 3E and fig. S5H). The sustained *HBZ* production in YS for several days before liver bud formation (4 PCW) was consistent with a scenario where the YS supports initial erythropoiesis. At 7 PCW, the embryonic liver contained both *HBZ* and *HBG1* (Fig. 3E), in keeping with previous studies of Hb switching (8). By 8 PCW, embryonic liver erythroblasts expressed *HBZ*-repressors and were *HBG1*-dominant, as we have previously shown (10). By contrast, the mouse liver was macroscopically red before AGM maturation (Fig. 3D). Tracking Hb subtype usage in the mouse, we noted two waves of pre-AGM erythropoiesis—an initial wave with *Hbb-y* and *Hba-x* transitioning to *Hba-a1/2*, and a second wave mirrored in both the YS and the torso or liver

Fig. 2. Multiorgan functions of YS.

(A) Dot plot showing the mean expression (color) and proportion of YS and liver stromal cells (dot size) expressing stromal DEG markers (data S3, S7, and S21). YS scRNA-seq data include main and gastrulation (gastr.) data. Liver scRNA-seq data include matched embryonic, fetal, and adult liver.

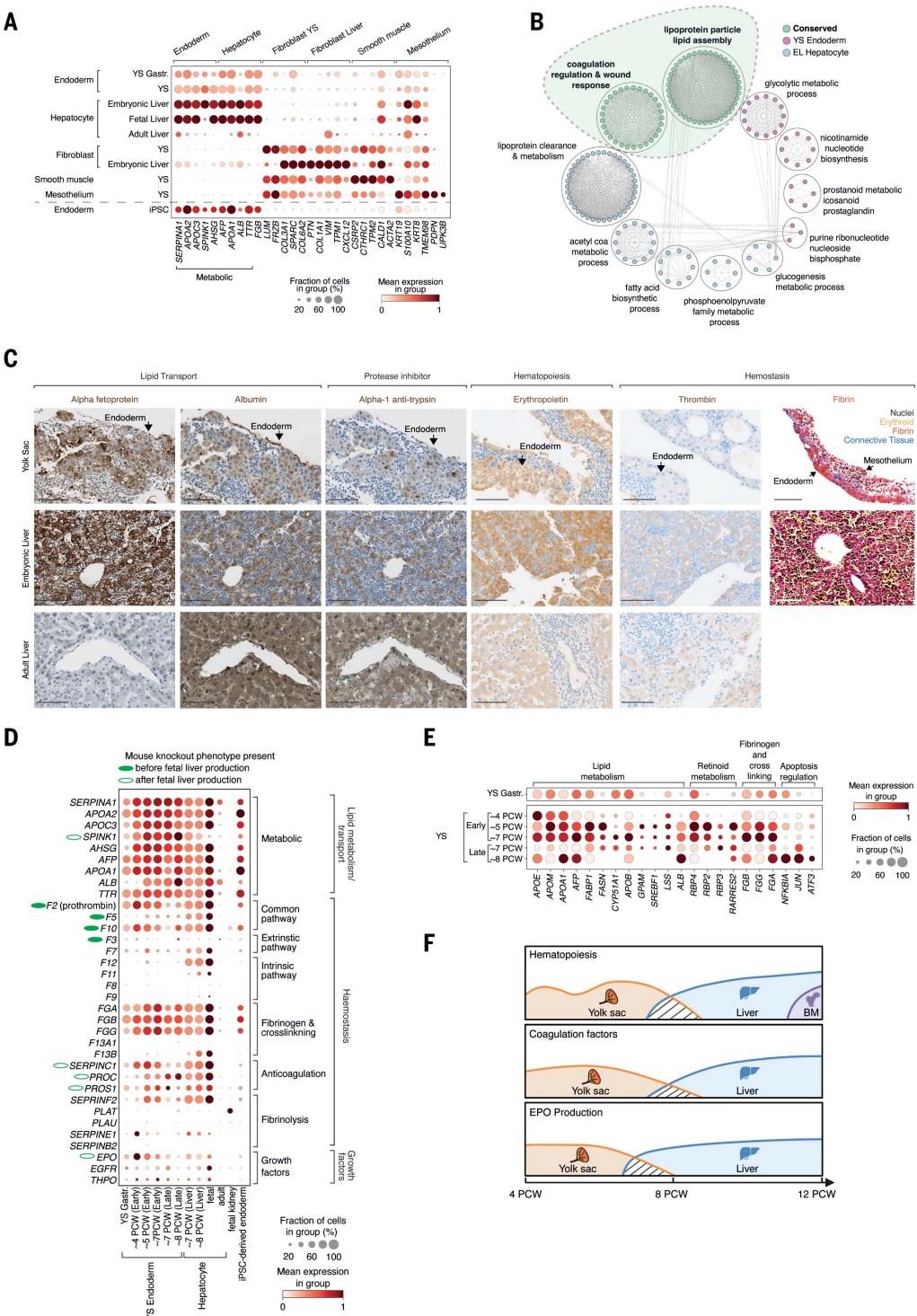
(B) Flower plot illustrating significantly enriched pathways in YS endoderm (pink) and embryonic liver (EL) hepatocytes (blue). Conserved pathways between tissues are highlighted in green and a dashed outline (data S25).

(C) (Columns 1 to 3) IHC staining of alpha fetoprotein (AFP), albumin (ALB), and alpha-1 antitrypsin (*SERPINA1*) in 8-PCW YS (top), EL (middle), and adult liver (bottom). Representative images of $n = 5$ YS (4 to 8 PCW), $n = 3$ ELs (7 to 8 PCW), and $n = 3$ adult liver samples. (Columns 4 and 5) IHC staining of EPO and thrombin (F2) in 7-PCW YS (top), 7-PCW EL (middle), and healthy adult liver (bottom). Representative images from $n = 3$ samples per tissue: YS (4 to 7 PCW) and EL (7 to 12 PCW). Proteins are brown, and nuclei are blue. (Column 6) Martius scarlet blue (MSB)-stained 8-PCW EL (representative of $n = 3$) and 4-PCW YS (representative of $n = 3$). Nuclei are gray, erythroid is yellow, fibrin is red, and connective tissue is blue (data S23). Scale bars, 100 μ m.

(D) Dot plot showing the mean expression (color) and proportion of cells in YS endoderm; embryonic, fetal, and adult liver hepatocytes; and stromal cells from fetal kidneys. Brackets indicate enriched GO annotations. Green ellipses denote genes with prenatal phenotypes in homozygous-null mice. Solid and hollow green outlines denote phenotype onset before and after fetal liver (FL) function, respectively, as per fig. S4E (data S25).

(E) Dot plot showing the mean expression (color) and proportion of cells expressing Milo-derived DEGs across gestation (dot size) in YS endoderm (data S24). Genes are grouped by function.

(F) Schematic of the relative contributions of YS (orange), liver (blue), and BM (purple) to hematopoiesis, coagulation factor, and EPO production in the first trimester of human development.



(*Hbb-bt1* and *Hbb-bs*) (fig. S5, G to I). Thus, there is a species-specific difference in YS erythropoiesis and a rapid shift in Hb usage after AGM development in humans.

We examined data from human gastrulation (~2 to 3 PCW) and CS10 to CS11 (~4 PCW)—time points before AGM-HSPC formation—to explore the differentiation potential of early HSPCs. At gastrulation, the YS hematopoietic

landscape had a tripartite differentiation structure, with erythroid, MK, and myeloid differentiation (Fig. 3F). This structure was also observed in the mouse YS (fig. S6, A and B, and data S5 and S11). Differential fate-prediction analysis demonstrated that early HSPCs pre-AGM at CS10 to CS11 (~4 PCW) were myeloid-biased, consistent with previous observations (9). However, the abundance of differentiating

erythroid and MK cells at CS10 to CS11 suggested that an earlier wave of erythroid and MK production had occurred (Fig. 3G and fig. S6C). Post-AGM, the model predicted that remaining early HSPCs were erythroid- and MK-biased, whereas definitive HSPCs were lymphoid- and MK-biased (Fig. 3G). This was in keeping with the first appearance of YS lymphoid cells (ILC progenitors, NK cells, and B lineage cells)

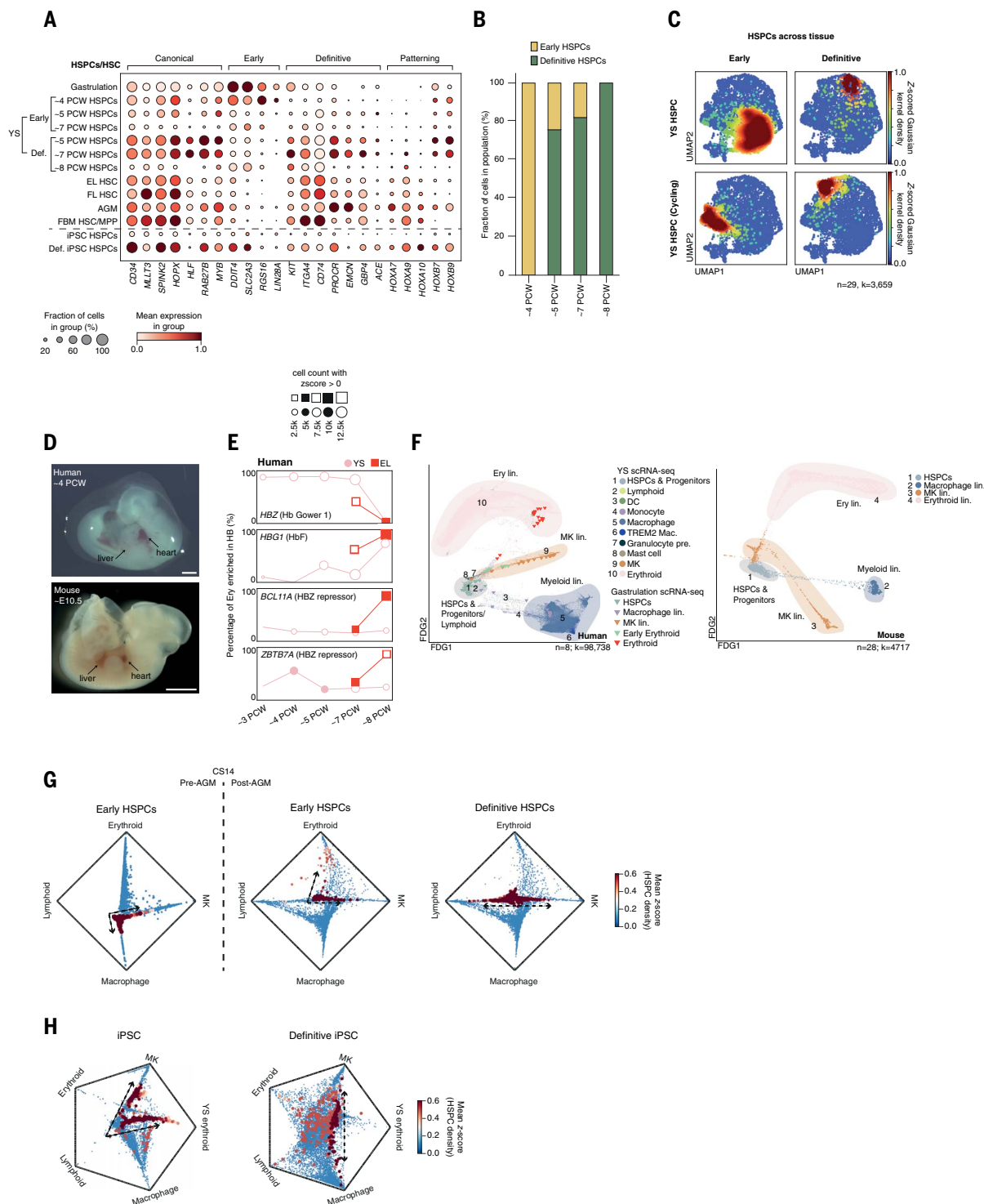


Fig. 3. Early versus definitive hematopoiesis in the YS and liver. (A) Dot plot showing mean expression (color) and proportion of cells expressing selected HSPC genes (dot size) in HSPCs from YS [main and gastrulation (14)], liver [EL and FL (10)], AGM (76), BM (34), and iPSC cultures [iPSC (20) and definitive HSPCs (12)]. (B) Bar chart showing proportion of early (yellow) to definitive HSPCs (green) in the YS scRNA-seq data grouped by gestational age. (C) Density plots showing YS HSPC (top) and cycling HSPC (bottom) with early (left) and definitive signatures (right) in an integrated landscape as per (A). Color indicates population z-scored KDE (data S5). Tissue contributions are shown in fig. S5E. (D) Representative image of whole ~4-PCW or CS12 human

(top; $n = 4$) and ~E10.5 or CS12 mouse embryo (bottom). Scale bars, 1 mm. (E) Line graphs showing change in erythroid cell proportion (y axis) enriched in globin gene expression across gestational age. Colors indicate scRNA-seq dataset: pink, human YS; red, matched EL. Shape size indicates cell count, scale indicates representative counts, and no shape indicates a count <500. Globins are grouped by roles in early or definitive hematopoiesis and repression. (F) FDG of hematopoietic cell states in the YS scRNA-seq data ($n = 8$, $k = 98,738$; dots) integrated with human gastrulation (14) scRNA-seq data ($n = 1$, $k = 91$; triangles) (left) and equivalent cell states in the mouse gastrulation scRNA-seq dataset (75) ($n = 28$, $k = 4717$; dots) (right). Colors represent cell

states, and clouds mark lineages. (G) Radial plots showing lineage transition probabilities between pre-AGM (CS10 to CS11; left) and post-AGM (>CS14; right) YS early and definitive HSPCs. Color indicates population z-scored KDE. Density position indicates respective lineage priming probability between macrophage, lymphoid

(NK and B lineage), erythroid, and MK terminal states. Arrows indicate proposed lineage priming based on KDE. (H) Radial plots showing lineage transition probabilities between iPSC-derived HSPCs (left) and definitive iPSC-derived HSPCs (right). Interpretation as in (G), with addition of embryonic erythroid terminal state.

post-CS14 (Fig. 1G). Differential fate-prediction analyses suggested that iPSC-derived HSPCs were embryonic erythroid-, myeloid-, and MK-biased, whereas definitive iPSC-derived HSPCs were lymphoid-, MK-, erythroid-, and myeloid-primed, consistent with the predicted lineage potential of their *in vivo* early and definitive counterparts (Fig. 3H and fig. S6D).

The life span of YS HSPCs

HSPCs arise from hemogenic endothelium (HE) in the aorta, YS, BM, placenta, and embryonic head in mice (26–30). In the human AGM, definitive HSPCs emerge from *IL33*⁺*ALDH1A1*⁺ arterial endothelial cells (AECs) via *KCNK17*⁺*ALDH1A1*⁺ HE (31). Dissecting YS endothelial cell (EC) states in greater detail, the broad category of PLVAP⁺ ECs included AECs and HE, whereas LYVE1⁺ ECs encompassed sinusoidal, immature, and Von Willebrand factor (VWF)-expressing ECs (Fig. 4A; fig. S7, A and B; and data S4 and S5). HE was a transient feature of early YS (Fig. 4A). Along inferred trajectories, YS HSPCs appeared to arise from AECs via HE as in AGM (12), sequentially up-regulating expected genes such as *ALDH1A1* (32) (Fig. 4B). The same EC intermediate states and transition points were identified in both iPSC culture systems (Fig. 4B and fig. S7C). In keeping with their more recent endothelial origin, we found that YS HSPCs and AGM HSPCs, but not embryonic liver or fetal BM HSPCs, retained an EC gene signature characterized by the expression of *KDR*, *CDH5*, *ESAM*, and *PLVAP* (Fig. 4C).

Receptor-ligand interactions capable of supporting HSPC expansion and maintenance in YS were predicted using CellPhoneDB (33) and compared with predictions in fetal BM (34). We identified YS ECs, fibroblasts, smooth muscle cells, and endoderm as likely interacting partners (Fig. 4, D to F, and data S28). YS ECs, like fetal BM ECs, were predicted to maintain and support the HSPC pool (35) through the production of stem cell factor (*KITLG*) and *NOTCH1/2*, although the repertoire of NOTCH ligands diverged between tissues (*DLL1* and *JAG1* in YS and *DLK1*, *JAG1/2*, *NOV*, and *DLL4* in BM) (Fig. 4D). The YS endoderm was predicted to support HSC pool expansion (36) through *WNT5A* signaling to *FZD3*. *WNT5A* was also expressed by a wide range of BM stromal cell types, but BM HSPCs were predicted to respond via *FZD6* rather than *FZD3*. All YS stromal fractions contributed to the extracellular matrix, which provides a substrate for adhesion but also modifies HSPC function, with *FN1* (from all fractions) potentially expanding the HSPC pool and *VTN* (from the

endoderm) contributing to long-term HSC-like quiescence (Fig. 4, D and F) (37, 38). Although BM HSPCs were also predicted to adhere to extracellular matrix proteins, the integrins and matrix constituents differed. The YS endoderm was predicted to form interactions with HSPCs via *EPO*, which may influence the fate of differentiating progenitors (39), and *THPO*, which supports HSC quiescence and adhesion in BM (40). No BM stromal source of *EPO* or *THPO* was detectable in our data, however (10, 34). Thus, these anatomically different hematopoietic tissues use similar pathways to support HSPCs, albeit with tissue-specific components.

YS HSPC receptor to stromal ligand interactions diminished between CS17 and CS23 (4 to 8 PCW), including the loss of cytokine and growth factor support and the loss of *TGFB1*, *WNT*, and *NOTCH2* signals (Fig. 4E, fig. S7E, and data S29). In many interactions, there was a reduction in HSPC receptor expression as well as stromal ligand expression (Fig. 4E; fig. S7, D and E; and data S29); yet, ligands were still expressed in age-matched liver and AGM stromal cells (fig. S7F and data S29). Adhesive interactions in the YS were also predicted to be significantly modulated (fig. S7, F and G, and data S29). Although aged-matched liver provided opportunities for adhesion with stromal cells, the AGM did not (fig. S7F and data S29). YS interactions gained between CS17 and CS23 included endoderm-derived *IL13* signaling to the *TMEM219*-encoded receptor implicated in the induction of apoptosis (Fig. 4D). Although limited conclusions can be made from studying cells that passed quality control for cell viability, we did observe up-regulation in proapoptotic gene scores in late-stage YS HSPCs, both early and definitive (fig. S7H).

Despite a marked change in the stromal environment of the later stage YS, the proportion of HSPC to cycling HSPC remained stable (fig. S5F). Differential lineage priming analysis revealed that very few HSPCs remained in CS22 to CS23 (8 PCW) YS, and most cells were terminally differentiated (fig. S6C). Thus, it is likely that an early burst of early HSPC production arises from transient YS HE, a later influx of definitive HSPCs derives from AGM, and a loss of stromal support between 6 and 8 PCW results in apoptosis and depletion of remaining HSPCs by terminal differentiation.

An accelerated route to macrophage production in YS and iPSC culture

Although YS hematopoietic progenitors are restricted to a short time window in early gestation, mouse models suggest that they con-

tribute to long-lived macrophage populations in some tissues (41). By scRNA-seq, transcriptionally similar macrophage populations can be identified in the YS and fetal brain before the emergence of definitive HSPCs (9). In our previous work, $k = 6682$ YS macrophages resolved into two subgroups (10). By contrast, our integrated dataset of $k = 45,118$ YS macrophages in the current study revealed a greater heterogeneity, including premacrophages, *CIQA/B/C*- and *MRC1*-expressing macrophages, and a rare *TREM2*⁺ macrophage subset (fig. S8A). Promonocytes expressing *HMGB2*, *LYZ*, and *LSP1* and monocytes expressing *S100A8*, *S100A9*, and *MNDA* were also detected (fig. S8A). Monocytes were observed only after liver development and AGM-derived hematopoiesis at CS14 (~5 PCW), but premacrophages and macrophages formed as early as CS10 (~4 PCW) (Fig. 5A and fig. S8B). Although the potential of early YS HSPCs to differentiate into monocytes has been demonstrated *in vitro* (9), there were too few promonocytes and monocyte progenitors (MOPs) in our data before CS14 to reliably confirm this potential. We identified two populations of YS monocytes, which diverged in expression of adhesion molecules. YS monocyte 2 expressed adhesion molecules *ICAM3*, *SELL*, and *PLAC8* (Fig. 5B), which were also expressed on fetal liver but not YS HSPCs (fig. S5C). YS monocyte 2 had a high probability of class prediction against fetal liver monocytes (fig. S8C). Thus, monocyte 2 is likely a recirculating fetal liver monocyte, although sequential waves of monocytopoiesis occurring within the YS cannot be excluded. YS CITE-seq data were used to identify discriminatory markers (CD15 and CD43 for monocyte 1; CD9 and CD35 for monocyte 2) and provide protein-level validation for differential expression of *SELL* (CD62L) and CD14 (fig. S8D and data S20).

The YS premacrophage differentially expressed high levels of *PTGS2*, *MSL1*, and *SPLA1* as well as expressing progenitor genes (*SPINK2*, *CD34*, and *SMIM24*), macrophage genes (*CIQA* and *MRC1*), and *CD52*, which is typically associated with monocytes (fig. S8A). This YS premacrophage rapidly declined by 5 PCW (Fig. 5A) and had no equivalent in the embryonic liver (fig. S8C). k -nearest neighbor (KNN) graph-based FDG and partition-based graph abstraction (PAGA) suggested a direct monocyte-independent trajectory to YS macrophages before CS14 (Fig. 5C and data S5). In this pre-AGM trajectory, a transition from HSPC to premacrophages then macrophages (nodes 1, 5, and 6 in Fig. 5C, upper panel) fit with our predictions that pre-AGM HSPCs exhibit myeloid bias (Fig. 3G). After CS14,

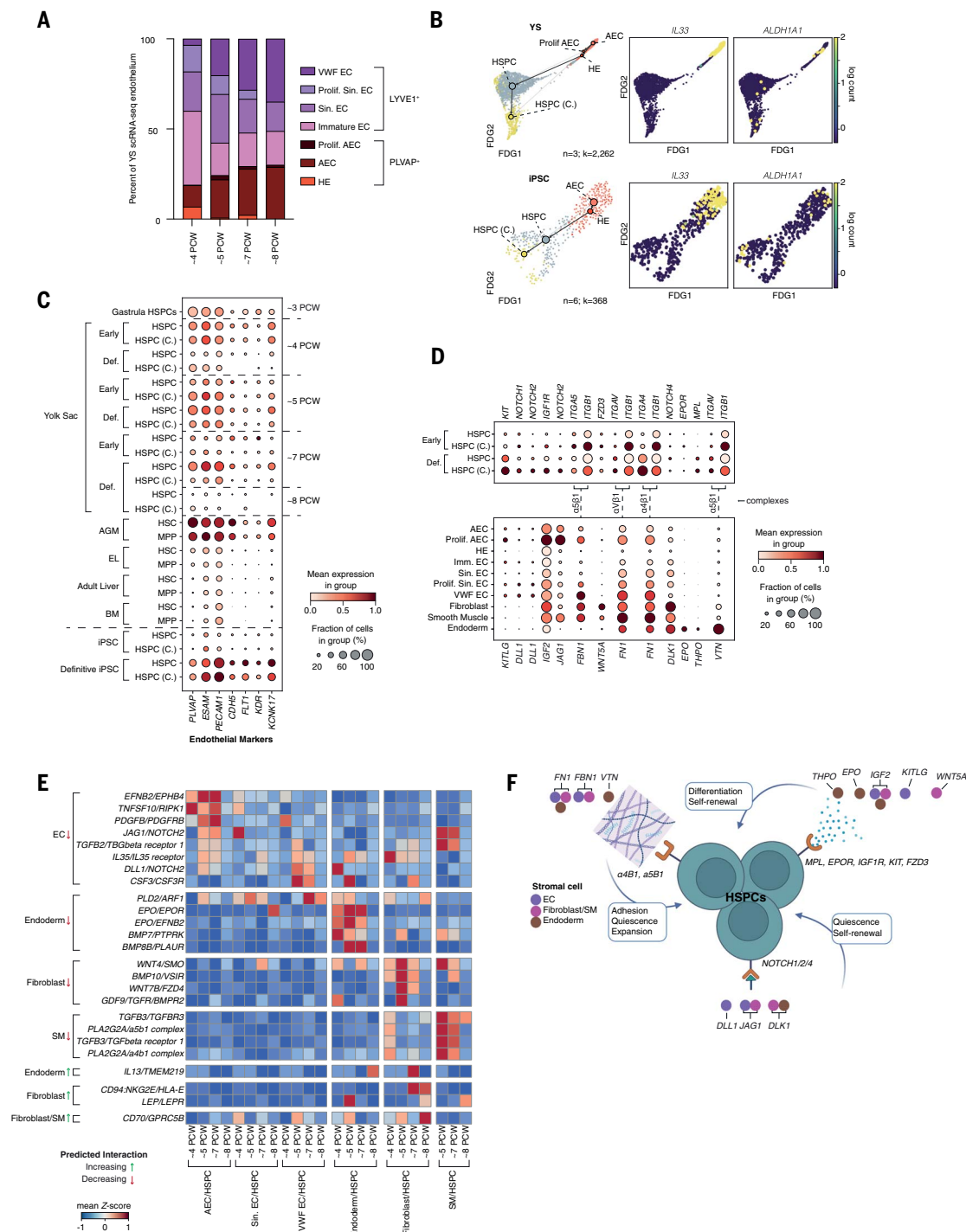


Fig. 4. The life span of YS HSPCs. **(A)** Bar chart showing the relative proportions of YS EC subsets by age (PCW). sin. EC, sinusoidal endothelial cells. **(B)** FDG overlaid with PAGA showing trajectory of HE transition to HSPC in YS scRNA-seq data ($n = 3$; CS10, CS11, and CS14; $k = 2262$) (top) and iPSC-derived HSPC scRNA-seq data ($n = 7$; $k = 437$) (20) (bottom), with feature plots of key genes (*IL33*, *ALDH1A1*) involved in endothelial to hemogenic transition (data S5). **(C)** Dot plot showing the mean expression (color scale) and proportion of cells expressing EC-associated genes (dot size) in HSPCs across gestational age (PCW). HSPCs are derived from YS (including gastrulation), AGM (12), matched EL and FL (10), fetal BM (34), iPSC-derived HSPC (20), and definitive iPSC-derived HSPC (12) scRNA-seq datasets. **(D)** Dot plot of the mean expression (color scale) and the fraction of cells expressing each gene (dot size) of curated genes predicted by CellphoneDB to form statistically significant ($P < 0.05$)

protein-protein interactions between HSPCs (top) and stromal cells (bottom) across all time gestational points. Brackets indicate which protein counterparts form complexes (data S29). Data are log-normalized, variance-scaled, and min-max-standardized with a distribution of 0 to 1. **(E)** Heatmap showing curated and statistically significant ($P < 0.05$) CellphoneDB-predicted interactions between YS HSPCs and stromal cells that change across gestation. Color scale indicates relative mean expression z-scores. **(F)** Schematic of selected and statistically significant ($P < 0.05$) CellphoneDB-predicted interactions between YS HSPCs and endoderm, fibroblasts (Fib), smooth muscle cells (SMCs), or EC derived from scRNA-seq data. Interactions are grouped by predicted receptor to ECM interactions, ligand-receptor interactions, and surface-bound ligand-receptor interactions. Receptors and ligands in *italics* significantly decrease at CS17 to CS23 (6 to 8 PCW) (data S28 and S29).

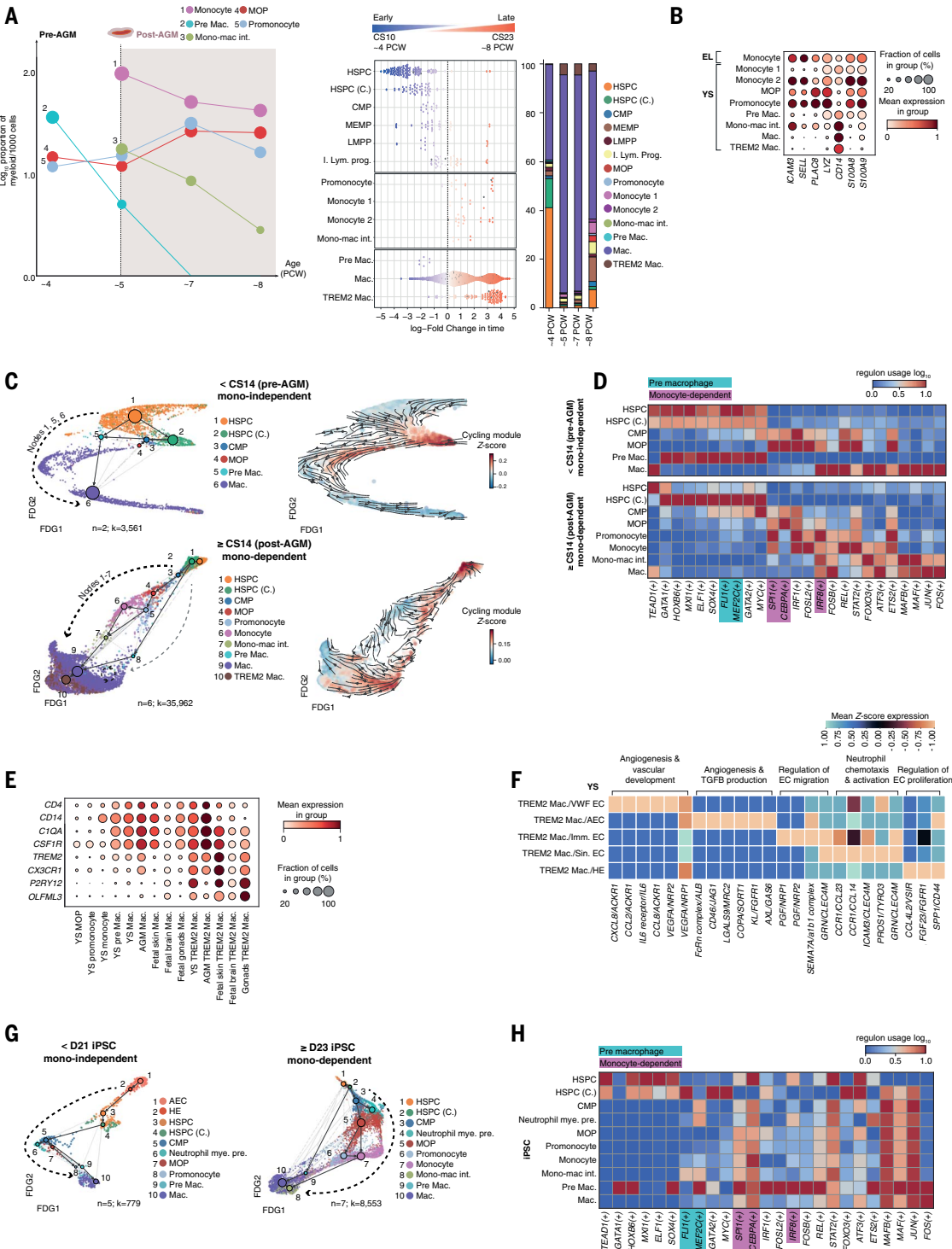


Fig. 5. Accelerated macrophage production in YS and iPSC culture.

(A) (Left) Line graph of monocyte and macrophage proportions in YS scRNA-seq across time. Dashed line indicates pre- and post-AGM stages. (Middle) Milo beeswarm plot showing differential abundance of YS scRNA-seq myeloid neighborhoods across time. Color shows degree of enrichment (blue, early; red, later) (data S4 and S24). (Right) Bar chart of YS scRNA-seq myeloid cell state proportions across time. Mono-mac int., monocyte macrophage intermediate. (B) Dot plot showing the mean expression (color) and proportion of cells expressing monocyte marker genes (dot size) in EL monocytes and YS myeloid cell states. Genes include YS versus EL monocyte DEGs and established

monocyte markers (data S17). (C) (Left) FDG of macrophage trajectory in YS scRNA-seq, colored by cell state, overlaid with PAGA showing monocyte-independent <CS14 (pre-AGM; $n = 2$; $k = 3561$; top) and monocyte-dependent trajectories >CS14 (post-AGM; $n = 6$; $k = 35,962$; bottom) (data S5). (Right) FDG overlaid with scVelocity directionality, colored by cell cycle gene enrichment (GO:000704 module). (D) Heatmap of regulons associated with trajectories in (C). TFs discussed in the text are highlighted (turquoise, premacrophage; purple, monocyte-dependent). (E) Dot plot showing the mean expression (color) and proportion of cells expressing macrophage and microglia marker genes (dot size) in myeloid cell states in YS, AGM (12), skin (48), gonad (49),

and brain (55) fetal scRNA-seq datasets (data S13 and S31). **(F)** Heatmap of significant ($P < 0.05$) CellPhoneDB-predicted interactions between YS scRNA-seq *TREM2*⁺ macrophages and ECs (data S28). Color represents z-scored expression of gene pairs, and brackets indicate top curated interactions for cell-state pairs. **(G)** FDG of macrophage trajectory in iPSC scRNA-seq (20)

colored by cell state, overlaid with PAGA showing monocyte-independent <D21 ($n = 5$; $k = 779$; left) and monocyte-dependent >D21 ($n = 7$; $k = 8553$; right) transitions (data S7 and S5). **(H)** Heatmap of regulons associated with iPSC macrophage trajectories shown in (G). TFs discussed in the text are highlighted, as in (D).

there was a clear differentiation trajectory from cycling HSPC to monocytes and monocyte-macrophages (nodes 1 to 7 in Fig. 5C, lower panel). After CS14, 15.33% of this macrophage pool was proliferating, and CellRank RNA state transition analysis was in keeping with active self-renewal (fig. S8E and data S5). Using PySCENIC, YS premacrophages were predicted to use a group of transcription factors (TFs), including *FLI1* and *MEF2C*, that have been reported in the differentiation of multiple lineages (42, 43). By contrast, the monocyte-dependent route (CMPs, MOPs, promonocytes, and monocytes) relied on recognized myeloid TFs such as *SPI1*, *CEBPA*, and *IRF8* (Fig. 5D and data S30).

TREM2⁺ macrophages expressed microglia-associated transcripts *CX3CR1*, *OLFML3*, and *TREM2* and were observed in the YS only after CS14 (Fig. 5, A, C, and E; fig. S8A; and data S13). By PAGA and CellRank state transition analysis, *TREM2*⁺ macrophages were closely aligned to the self-renewing macrophage population (Fig. 5C and fig. S8E). YS *TREM2*⁺ macrophages were located adjacent to the mesothelium, in a region enriched by ECs (fig. S8F). CellPhoneDB predicted interactions between *TREM2*⁺ macrophages and *VWFF*⁺ ECs via *CXCL8* and *NRP1*, both of which are involved in angiogenic pathways (44, 45) (Fig. 5F and data S28). *TREM2*⁺ macrophages also expressed the purinergic receptor *P2RY12*, which supports trafficking toward adenosine 5'-triphosphate (ATP)- or adenosine 5'-diphosphate (ADP)-expressing ECs, as reported in the mouse central nervous system (46, 47) (Fig. 5E and data S31). To establish whether *TREM2*⁺ macrophages are present in other fetal tissues, we assembled an integrated 12-organ developmental atlas (fig. S8G). We resolved six macrophage fractions based on harmonized cross-tissue definitions from our recent prenatal immune analysis (by label transfer): premacrophages and *TREM2*⁺ macrophages (as in our cluster-driven annotations) as well as LYVE1^{hi}, Kupffer-like, iron-recycling, and proliferating macrophages (48) (fig. S8, C and G to J, and data S5 to S7 and S17). *TREM2* is implicated in lipid sensing by anti-inflammatory tissue macrophages in the adult human and mouse (23–25), but we observed the highest expression of *TREM2* in macrophages bearing a microglia-like signature in developing tissues, including YS, skin [as previously reported (48)], gonads [as previously reported (49)], brain, and AGM but not BM, liver, kidney, thymus, mesenteric lymph nodes (MLNs), or gut (fig. S8, I and J, and data S31).

Next, we investigated whether transcriptional features of pre-AGM macrophages could be used to evaluate YS macrophage contribution to developing tissues. In our 12-organ macrophage dataset, pre-AGM macrophages were compared against post-AGM macrophages in an integrated variational-autoencoder (VAE) latent space using a Bayesian differential expression approach. The most predictive pre-AGM macrophage features comprised nine genes, including five genes in common with a TLF⁺ signature identified from cross-tissue analysis of mouse macrophages (*LYVE1*, *TIMD4*, *FOLR2*, *MRC1*, and *NINJ1*) (50) (fig. S9A and data S17). By KDE, macrophages significantly enriched in our pre-AGM module colocalized with LYVE1^{hi} macrophages from gonads, liver, skin, and AGM and with all macrophage fractions from the YS (fig. S9, B to D; fig. S8H; and data S7 and S32). The proportion of pre-AGM module-enriched macrophages trended downward over time, even in the brain (fig. S9E). By transcriptome alone, it was not possible to separate dilution by influx of non-YS macrophages from transcriptional adaptation to the tissue environment. With this caveat, we assembled a 20-organ, cross-tissue integrated landscape of adult tissue macrophages using publicly available single-cell data from the Human Cell Atlas and Tabula Sapiens (fig. S9, F to H, and data S6, S7, S14, and S17). Fat, vasculature, muscle, brain, and bladder had the highest proportion of macrophages enriched in the pre-AGM signature (fig. S9H and data S7).

We integrated our YS gene expression data with scRNA-seq data from iPSC-derived macrophage differentiation ($n = 19$; $k = 50,512$) (20) after refining the annotations of iPSC-derived cell states (fig. S10, A to C, and data S5 and S13). Nonadherent, *CD14*-expressing cells appearing after week 2 of differentiation expressed *CTQA*, *CTQB*, and *APOC1* in keeping with a macrophage identity, whereas *CD14*-, *CD52*-, *FCN1*-, and *S100A8/9*-expressing monocytes only emerged after week 3 (fig. S10, D and E). Before monocyte emergence, a monocyte-independent macrophage differentiation trajectory was observed, consistent with previous observations (20) (Fig. 5G and fig. S10C). TF regulatory profiles of iPSC-derived macrophage differentiation were consistent with both the premacrophage and monocyte-dependent TF profiles inferred from our YS data, including usage of *MEF2C*, *SPI1*, *CEBPA*, and *IRF8* in iPSC-derived premacrophages (Fig. 5H and data S30). However, neither iPSC culture system could recapitulate the heterogeneity of macrophages seen in native tissues

(fig. S10E), which suggests that interactions with stromal cells, such as ECs, may be required to acquire specific molecular profiles.

Discussion

Using single-cell multiomic and imaging technologies, we delineate the dynamic composition and functions of human YS in vivo from 3 PCW, when the three embryonic germ layers form, to 8 PCW, when most organ structures are already established (21). Although the scarcity and small sample size necessitated a primarily computational approach, we deliver a comprehensive resource. LR and VAE models provided by our data will facilitate future use of our YS atlas to map scRNA-seq datasets (51, 52), empowering future mechanistic perturbation and lineage-tracing experiments in iPSCs and model systems.

We detail how the YS endoderm shares metabolic, biosynthetic, and erythropoiesis-stimulating functions with the liver. In part, this shared functionality may relate to their common role in creating a hematopoietic niche (53). We identify differences in the handover from YS to liver hematopoiesis between species. In mice, erythroid progenitors in the YS mature before the onset of circulation, but erythromyeloid progenitors can exit the YS and mature in the fetal liver, giving rise to long-lived populations, such as fetal liver monocyte-derived macrophages. We show that in human YS, active differentiation of erythroid and macrophage cells occurs for several weeks before liver handover; and, at least in terms of erythropoiesis, there is a rapid transition from YS erythroid production to embryonic liver erythroid production shortly after AGM-derived HSPCs emerge. In a landmark study on human Hb switching, directly labeled 6-PCW liver and YS erythrocytes contained embryonic Hb subunits (ϵ and ζ), but colonies derived from liver and YS progenitors at this time produced fetal Hb subunits (α and γ) (8). This is in keeping with YS-derived erythrocytes recirculating throughout the embryo and membranes while a post-AGM progenitor is preparing for liver erythropoiesis. Direct evidence that human liver erythropoiesis is supplied predominantly from AGM-derived HSPCs rather than a YS-derived EMP-like progenitor is still lacking. Future studies are needed to examine the handover of macrophage production from early to definitive sources in humans, which may question the primacy of mouse models of early myelopoiesis. A more expansive species reference, including rabbits with their greater early gestational similarity to humans,

will facilitate selection of appropriate models for genetic manipulation and functional validation (54).

The developmental window investigated in this work encompasses hematopoiesis from HSPCs arising both within the YS and within the embryo proper. We reconstructed YS HSPC emergence from a temporally restricted HE, featuring similar transition states and molecular regulation to AGM HSPCs. By gastrulation (CS7; 2 to 3 PCW), YS HSPCs already differentiate into erythroid, MK, and myeloid lineages. Building on a recent compilation of gene scorecards that characterize early and definitive HSPCs (12), we were able to parse the two fractions and document the transition to definitive HSPC dominance after CS14 (~5 PCW). This separation also allowed us to identify an early HSPC bias toward myeloid, erythroid, and MK lineages and a definitive HSPC bias toward MK and lymphoid lineages. Both early and definitive YS HSPCs became more quiescent and up-regulated apoptosis-related genes between CS17 and CS23 (~6 to 8 PCW). Stromal cell ligands predicted to support HSPCs were markedly disrupted during this time, which suggests that the barriers to YS HSPC survival may be extrinsic.

Early HSPCs use an accelerated route to macrophage production independent of monocytes. Both accelerated and monocyte-dependent macrophages were recapitulated during in vitro differentiation of iPSCs, but diverse macrophage subtypes, such as *TREM2*⁺ macrophages, were not. *TREM2*⁺ macrophages, which are transcriptionally aligned with brain microglia, fetal skin, testes, and AGM *TREM2*⁺ macrophages, were predicted to interact with ECs, potentially supporting angiogenesis, as has been described in the mouse brain (55).

There is a growing appreciation of the potentially life-long consequences of early developmental processes. Our study illuminates a previously obscure phase of human development, where vital organismal functions are delivered by a transient extraembryonic organ using noncanonical cellular differentiation pathways that can be leveraged for tissue engineering and cellular therapy.

Materials and methods

Ethics and sample acquisition

Tissues were obtained from the MRC–Wellcome Trust-funded Human Developmental Biology Resource (HDBR; <https://www.hdb.org>) with appropriate written consent and approval from the Newcastle and North Tyneside NHS Health Authority Joint Ethics Committee (18/NE/0290). HDBR is regulated by the UK Human Tissue Authority (HTA; www.hta.gov.uk) and operates in accordance with the relevant HTA Codes of Practice. Tissues used for light-sheet fluorescence microscopy were obtained through INSERM's HuDeCa Biobank and made

available in accordance with the French bylaw (Good practice concerning the conservation, transformation and transportation of human tissue to be used therapeutically, published on 29 December 1998). Permission to use human tissues was obtained from the French agency for biomedical research (Agence de la Biomédecine, Saint-Denis La Plaine, France).

Embryos were staged using the Carnegie staging method (56). A piece of skin or chorionic villi tissue was collected from each sample to perform quantitative PCR karyotyping of sex chromosomes and autosomal chromosomes 13, 15, 16, 18, 21, and 22 for the most commonly seen chromosomal abnormalities. No abnormalities were detected.

Processing samples for imaging and single-cell sequencing

Tissues were transported in phosphate-buffered saline (PBS) on ice, were dissected within 24 hours, and were processed immediately (<1 hour after dissection). For formalin-fixation and paraffin-embedding, samples were immediately placed in 10% (w/v) formalin. Processing and embedding were performed by NovoPath, Newcastle upon Tyne NHS Trust. For RNAscope, samples were snap-frozen in an isopentane bath in liquid nitrogen before embedding in optimal cutting temperature (OCT) compound. Single-cell suspensions were generated by dicing tissue into segments <1 mm³, followed by enzymatic digestion for 30 min at 37°C with intermittent shaking. Digestion media was 1.6 mg/ml collagenase type IV (Worthington) in RPMI (Sigma-Aldrich) supplemented with 10% (v/v) heat-inactivated fetal bovine serum (FBS; Gibco), 100 U/ml of penicillin (Sigma-Aldrich), 0.1 mg/ml of streptomycin (Sigma-Aldrich), and 2 mM L-glutamine (Sigma-Aldrich). Digested tissue was passed through a 100-μm filter, and cells were collected by centrifugation (500g for 5 min at 4°C). Cells were treated with 1X red blood cell (RBC) lysis buffer (eBioscience) for 5 min at room temperature and washed once with Flow Buffer [PBS containing 5% (v/v) FBS and 2 mM EDTA] before counting. Processing for scRNA-seq was continued promptly on fresh cells, for other uses (including CITE-seq) cells were collected by centrifugation (500g for 5 min at 4°C) and resuspended in 10% (v/v) dimethyl sulfoxide (DMSO) in FBS for freezing. For light-sheet fluorescence microscopy, tissues were fixed in 4% paraformaldehyde (PFA) and dissected. Gestational age was then estimated as previously described (57).

Processing of single-cell suspensions for scRNA-seq

Immediately after isolation and counting, cells were collected by centrifugation (500g for 5 min at 4°C) and resuspended in a residual buffer. Three microliters of CD45 BUV395 (clone: HI30, BD Biosciences) was added to the resuspended cells and incubated on ice in the dark for 30 min,

washed with Flow Buffer and resuspended at ~1 × 10⁷ cells/ml. Immediately before sorting, cells were passed through a 35-μm filter (Falcon) and 4',6-diamidino-2-phenylindole (DAPI) (Sigma-Aldrich) was added at a final concentration of 3 μM. Flow sorting was performed on a BD FACSaria Fusion instrument using DIVA v.8, and data were analyzed using FlowJo (v.10.4.1, BD Biosciences). Cells were gated to exclude dead cells and doublets, and then isolated for scRNA-seq analysis (droplet-based 10x Genomics, or plate-based Smart-seq2) using a 100-μm nozzle. For droplet-based scRNA-seq, CD45⁺ and CD45[−] cells were sorted into separate chilled FACS tubes coated with FBS and prefilled with 500 μl of sterile PBS. For plate-based scRNA-seq, CD45[−] AF⁺ SSC⁺⁺ single cells were index-sorted into 96-well LoBind plates (Eppendorf) containing 10 μl of lysis buffer [TCL (Qiagen) + 1% (v/v) β-mercaptoethanol] per well.

Library preparation and sequencing of scRNA-seq and CITE-seq samples

For the droplet-based scRNA-seq experiments, cell suspensions isolated by FACS were counted and loaded onto the 10X Genomics Chromium Controller to achieve a maximum yield of 10,000 cells per reaction. 5' V1 kits were used and sequencing libraries were generated according to the manufacturer's protocols. Libraries were sequenced using either an Illumina HiSeq 4000 or NovaSeq 6000 to generate at least 50,000 raw reads per cell.

For the plate-based scRNA-seq experiments, the frozen cell lysates were thawed on ice for 1 min. Purified cDNA was generated and amplified using a modified Smart-seq 2 protocol described in Villani *et al.* (58). Sequencing libraries were then generated using Illumina Nextera XT kits with v2 index sets A, B, C, and D. 384 cells were pooled and were sequenced using a HiSeq 4000 to generate at least 1 × 10⁶ raw reads per cell.

For the CITE-seq experiments, frozen cells were thawed, counted, and pooled. Fc blocking reagent (Biolegend) was added to the cell pools and left to incubate at room temperature for 10 min. Five hundred nanoliters of CD34 APC/Cy-7 (clone: 581, Biolegend) was then added to the Fc-blocked cells and left to incubate in the dark and on ice for 10 min. During this incubation, the CITE-seq antibody cocktail (Biolegend) (see data S33) was centrifuged at 14,000g for 1 min. Flow buffer was then added to reconstitute before incubating for 5 min at room temperature. The resuspended antibody cocktail was then centrifuged at 14,000g for a further 10 min before adding to the cells. The cells and CITE-seq antibody cocktail were then left to incubate for 30 min in the dark and on ice. After this time, the cells were washed twice with Flow buffer and resuspended in a final concentration of 50 μg/ml of 7 AAD (Thermo Fisher Scientific) in Flow buffer.

Live, single cells or live, single CD34⁺ cells (for the CITE-seq experiments) were then isolated by FACS into 500 µl of PBS in FACS tubes coated with FBS. Cells were then counted and submitted to the CRUK CI Genomics Core Facility for subsequent processing using 10x Genomics protocols and sequencing. Single-cell gene expression and cell surface protein libraries were generated using single-cell 3' v3 kits according to the manufacturer's protocol. Libraries were sequenced using a NovaSeq 6000 to achieve a minimum of 20,000 reads per cell for gene expression and 5000 reads per cell for cell-surface protein.

Alignment, quality control, filtering, and preprocessing of scRNA-seq and CITE-seq data

scRNA-seq expression data (including droplet-based and plate-based) were mapped with Cell Ranger (version 3.0.2) to a human reference genome (see data S1) and low-quality cells expressing <2000 reads, <200 genes, and >20% mitochondrial reads were filtered out of the data. Data on genes expressed in fewer than three cells was removed.

For droplet-based scRNA-seq data, the following additional QC steps were performed. Scrublet (59) v0.2.3 was applied to each sequencing lane for doublet detection, and clusters with > [median + (1.48 × MAD)] (where MAD is the median absolute deviation) of the median cluster doublet detection score were removed (data S3). Ambient RNA was removed with Cellbender (v0.2.0) with false discovery rate (FDR) = 0.01 and epochs = 150 (60). To determine likelihood of maternal contamination, data were pooled by donor and submitted to Souporecell (v2.4.0) at genotype clusters $k = 1$ and $k = 2$ models to represent likelihood of no maternal contamination and possible maternal contamination, respectively. The optimal model was identified via BIC (Bayesian Information Criterion), where we observed a smaller BIC index at $k = 2$ in one donor (F37, Female, 5 PCW). Cells from the F37 alternate genotype were identified as potential maternal contaminants, composed mainly of monocytes ($n = 149$), and monocyte-macrophage intermediates (monomac int.) ($n = 25$), and excluded from downstream analysis.

For CITE-seq data, FASTQ alignment was performed for multiplexed RNA lanes with Cell Ranger (v4.0.0) and GRCh38-2020-A reference genome, and for multiplexed protein lanes with CITE-seq-Count (v1.4.3). Lanes with cells pooled from multiple donors were deconvoluted using Souporecell singularity image at <https://github.com/wheaton5/souporecell>. Low-quality cells expressing <200 genes and >20% mitochondrial reads were removed, and doublets were removed by applying Scrublet v0.2.3 to each sequencing lane and then removing clusters with > [median + (1.48 × MAD)] of the

median cluster doublet detection score. CITE-seq protein data underwent QC and preprocessing as previously described (34) (i.e., cells were first filtered to intersect barcodes with counterpart CITE-seq RNA data, then unmapped antibodies were filtered out, and then protein cells were filtered for low quality by cells with <30 proteins and expressing >5000 reads) (data S4, S19, and S22).

scRNA-seq count matrix transformation, normalization, and preprocessing were performed using Scanpy (61) (v1.9.0) in python (v3.8.6). We normalized raw gene counts using the *sc.pp.normalize_total* function (*target_sum = 10e4*) and performed $\ln(x)+1$ transformation. Reported expression values were normalized, log-transformed, and scaled to variance of mean using the *sc.pp.scale* function independently for each analysis.

For CITE-seq data count matrix transformation, we first performed denoised and scaled by background (DSB)-normalization and applied a Gaussian mixture model (GMM) for background nonspecific binding signal regression per sample as previously described (62). For the first step, a modified DSB-normalization approach used in our previous study (34) was constructed. For each CITE-seq lane, low-quality/empty droplets were identified as droplets under the largest UMI peak which had a value <1.96 × standard deviations (std) of the mean UMI counts value (mu_UMI) per sample. Peak detection was conducted using the *scipy.signal.find_peaks* function. The number of peak detection bins were dynamically estimated as $\lceil 3.322 \times \log(X) \rceil$, where X was the total number of droplets. The model iterated through a series of 20 prominence intervals (0 to 20) with widths (0 to 10) where peaks detected < [mu_UMI - (1.96 × std)] were retained as empty droplet peaks. In cases where no empty droplet peaks were detected, the empty droplet threshold was taken to be < [mu_UMI - (1.96 × std)]. The estimated empty droplets matrix was then taken into downstream DSB normalization in the same way as our previous study (34). For the second step of CITE-seq matrix transformation, we trained a GMM to model the variance of protein expression levels in each cell. We used the *sklearn* (v1.1.3) *sklearn.mixture.GaussianMixture* module to fit 20 models with an increasing number of cell clusters k (between $k = 2$ and $k = 21$) to represent expression patterns of each protein by cell. The optimal model was identified using BIC ($BIC_i = 2L_i + k_i \log n$) and AIC (Akaike information criterion) ($AIC_i = 2L_i + 2k_i$) metrics, where k is the number of GMM cell protein expression clusters, n is the number of cells in the sample, and L is the model log likelihood. The models with the best performing BIC and AIC scores were selected. The mean expression values of GMM clusters with lowest expression values from each GMM model were interpreted as mean

background expression per protein. Background-signal regression was then carried out using a Gaussian linear model (GLM) per protein, constructed using the *GLM* function from *statsmodels* (v0.13.5) on standardized, per-cell background scores (BG_score). Per-cell background scores were defined by taking the euler number I to the power of each protein background mean (μ_{bg}), divided by e to the power of the protein expression in each cell (x), then scaled to a distribution between 0 and 1 by subtracting the minimum score and subsequently dividing by the maximum score. Background scores inversely correlate with the magnitude of background expression per cell. $BG_score = [\text{score} - \min(e^{\mu_{bg}}/e^x)] / \max(e^{\mu_{bg}}/e^x)$. The per-cell background signal regressed counts were used for subsequent analyses, interpretation, and visualization. Cells comprising the empty droplet matrix were removed and were not considered for downstream analyses.

Integration and batch correction of scRNA-seq and CITE-seq datasets

For integration of newly generated YS scRNA-seq data with external datasets, Cell Ranger count was first reapplied for the alignment of CS10/CS11 and CS14 embryonic YS scRNA-seq data previously acquired (12, 63) (data S1). The following steps were then followed for the total integrated YS droplet-based scRNA-seq dataset. Highly variable gene (HVG) selection was performed using the *sc.pp.highly_variable_genes* function (*min_mean = 0.001*, *max_mean = 10*) for embedding by dispersion. Dimensionality reduction and batch correction was carried out using the scVI module within *scvi-tools* (v0.19.0) (52) as used in *scvi-tools* (51) (HVG = 7500, *dropout_rate = 0.2*, *n_layer = 2*) with biological replicate taken as the technical covariate. To ensure model performance was optimal for each independent analysis, scVI was benchmarked against the python implementation of Harmony (64) (*Harmonypy* v0.0.5) at various theta values between 1 and 20. kBET (65) and Silhouette scores (*sklearn.metrics.sil_score*) were computed for each iteration between donor covariates and compared with the scVI integration. For integration of adult scRNA-seq data, publicly available single-cell and single-nuclei RNA-seq data of 20 healthy adult tissues (data S6 and S7) were integrated using scVI (HVG = 1500, *layers = 1*). Batch correction was conducted on donors, single cells or single nuclei, data source, number of genes, total counts, percentage of mitochondrial genes and ribosomal genes. See data S6 for information regarding external scRNA-seq datasets that have been incorporated and integrated in this study.

For multimodal integration of CITE-seq datasets, we compared the integration of both RNA and protein modalities using the *totalVI* module in *scvi-tools* (v0.19.0) against batch integration

using only the RNA modality the scVI module in scvi-tools. We performed *sc.pp.highly_variable_genes* function on RNA modality (HVG = 4000) accounting for FACs sampling and donor technical covariates. We then generated a multimodal totalVI VAE latent representation following totalVI pipeline (52). To benchmark performance between multimodal and single-modality scRNA-seq data integration, global silhouette distances between Leiden clusters ($res = 3$) derived from the multimodal totalVI VAE latent representation were compared against clusters derived from the scVI derived VAE representation as described above (HVG = 4000, dropout_rate = 0.2, n_layer = 2) (fig. S11A). Intersecting cells captured between protein and RNA modalities (by barcode) were considered in the totalVI integration (fig. S11, B to D, and data S4 and S22).

All scVI VAE and ldVAE models trained on the YS and integrated atlases are available on our data portal (see Data and materials availability) and will facilitate transfer learning for future reference mapping of scRNA-seq data with single-cell architectural surgery (scArches) (18).

Clustering and annotation of scRNA-seq and CITE-seq data

Clustering of scRNA-seq and CITE-seq datasets was performed using the Leiden algorithm (66) (*sc.tl.leiden*) with a resolution parameter of $res = 1.5$ (CITE-seq $res = 3$) on a KNN graph ($k = 30$ for scRNA-seq and $k = 15$ for CITE-seq) unless specified otherwise. To measure the effect of decreasing graph complexity on specific populations (YS scRNA-seq endoderm and IPSC-derived macrophages) and global population specificity and homogeneity in each independent analysis, the neighborhood graph complexity parameter (k) was benchmarked at value intervals between 5 and 50. Benchmarked metrics for population specificity included the adjusted mutual information score (MI) and adjusted Rand index (RAND). Metrics for population homogeneity included the silhouette index (SI) and within-cluster sum of squared errors (WSS) (fig. S12, A and B, and data S3 and S7). In cases where datasets are compared probabilistically, or where new classifications have been made, an implementation of low-dimensional ElasticNet regression (EN) (described in the “Cell state predictions using probabilistic low-dimensional ElasticNet regression” section of the Materials and methods) was used to first classify individual cells where a model-specific decision threshold of 0.9 was used for classification tasks. Cells classified inherited labels from the model trained on YS scRNA-seq data. Clusters were then assigned classes if the majority projected label had a label count distribution of $>[\text{mean} + (1 \times \text{std})]$ of label counts per cluster. Resultant cell state classifications were further manually checked using DEGs using the *sc.tl.rank_genes_groups* function in Scanpy which performed

a two-sided Wilcoxon rank-sum test for genes expressed in $>25\%$ of cells, with a log-transformed fold change cutoff of 0.25. All P values were adjusted for multiple testing using the Benjamini-Hochberg method. Annotation of YS and liver CITE-seq data was performed by training an EN model using YS and embryonic liver scRNA-seq datasets as references, respectively. These labels were then distributed by majority voting onto Leiden clusters derived from CITE-seq data (data S9 and S10). The resultant cluster annotations were validated using the same markers identified in matched RNA data and underwent additional manual annotation where required. For differential expression testing of surface proteins in multimodal CITE-seq data, we conducted a one_vs_all DE test using the *vae.differential_expression_module* within totalVI (Bayes factor > 3 , median LFC > 0.25). Marker proteins and corresponding populations were subsequently subject to hierarchical grouping using the *sc.tl.dendrogram* functionality within Scanpy (fig. S11, B to D, and data S4, S20, and S22). Bayesian differential expression testing between cell states in the integrated 12 fetal organ atlas was carried out using a scVI integrated latent VAE representation with a one_vs_all DE test using the *vae.differential_expression_module* within scVI (v0.19.0) (Bayes factor > 3 , median LFC > 4). Variation of effect sizes on state-specific normalized counts between latent variables in the integrated latent VAE representation were first modeled. The posterior likelihood of differential expression was attained by repeated one_vs_all sampling of the variational distribution. Significant features were defined with a likelihood of differential expression (Bayes factor) > 3 and median LFC > 4 . Bayesian differential expression testing between myeloid cell states in the integrated 20 organ adult scRNA-seq atlas was carried out as described above (fig. S12C and data S6, S7, and S17).

Dimensionality reduction and marker expression visualization

For visualization, the UMAP algorithm was run using the *sc.tl.umap* function in Scanpy. Dot-plots and violin plots were produced in Scanpy and all gene expression values displayed were normalized, log-transformed, and scaled as described in the preprocessing section unless otherwise stated. Dot plots that display data from multiple datasets used independent log-normalization, variance scaling, and min-max standardization to a distribution of 0 to 1 per dataset unless otherwise stated. FDGs computed with the *sc.tl.draw_graphs* function in Scanpy using the Force Atlas2 parameter were used to infer trajectories. PAGA were computed on the KNN graphs and overlaid onto FDGs where nodes represented the centroid of each cell state cluster and the thickness of edges represented the similarity between cell states (data S5).

Proportion line graphs for specific populations (e.g., erythroid cells) enriched in specific genes (e.g., *HBZ*) using the *sc.tl.enrich* function in Scanpy were produced using Matplotlib (v3.6.2). To ensure temporal changes in population size and background expression were accounted for, we segregated our population of interest by age and computed changes in relative population proportion enriched in each gene, only considering cells expressing >0 log-normalized counts for each gene. Enriched cells were defined with >0 score of each scored gene subtracted with the mean expression of a randomly sampled set of 200 selected reference genes at 50 bins using the aforementioned enrichment function in Scanpy. Proportions of enriched cells in each cell type compartment were then plotted as a discrete time series across gestational age to visualize differential enrichment of cells expressing the genes of interest. Data point sizes represented enriched cell counts. To aid interpretation, an ordinal scale of representative cell counts was included as a legend in the plots.

Proportions of specific populations (e.g., macrophages) enriched in specific gene modules (e.g., pre-AGM module) were visualized using violin graphs produced using Matplotlib and Seaborn (v0.12.1) python libraries. To ensure background expression profiles were accounted for, we segregated our population of interest and computed changes in relative population proportion enriched in each gene module. Significant module enrichment was defined as described above. Enriched cells from each cell type compartment were then graphed across organs. Enrichment scores were standardized to the median by subtraction of the median and subsequent division by MAD.

Differential abundance testing and FACS correction

We tested for differential cell-state abundance across gestation using the Milo framework (67), correcting for CD45 positive and negative FACS isolation strategies using a previously published technique (48). Where FACs correction was applied, we calculated a FACS isolation correction factor for each sample s sorted with gate i as $[\hat{p}_i = \log(p_i S / S_i)]$ where p_i is the true proportion of cells from gate i and S represents the total number of cells from both gates. A KNN graph was then constructed from the remaining cells using the *milopy.core.make_neighborhoods* function ($\text{prop} = 0.05$). Neighborhood labels were determined by majority voting of cell labels by frequency in each neighborhood ($>50\%$). The YS scRNA-seq data was then split into five age bins (3 PCW, 4 PCW, 5 PCW, 7 PCW, and 8 PCW) and cell counts were modeled as a negative binomial generalized linear model (NB-GLM) with Benjamini-Hochberg weighted correction as previously described (48). Significantly differentially abundant neighborhoods

were detected by SpatialFDR- (<0.1 , $\log FC < 0$) for early enriched neighborhoods and (<0.1 , $\log FC > 0$) for late neighborhoods (data S24).

Beeswarm plots were generated using the *ggplot2* library (v3.4.2). Each node represents an independent neighborhood of cells derived from the KNN graph. The x -axis position of each node represents the fold-change (positive or negative) associated with the distribution of age groups present in each neighborhood where larger proportions of older groups in a given neighborhood encourages a positive fold change and vice versa. Colored nodes represent neighborhoods with significant enrichment ($P < 0.05$ spatial FDR) and the intensity represents the degree of significance.

Clustered gene set enrichment analysis

We ranked conserved markers ($P < 0.05$) between the endoderm cell state in YS scRNA-seq data against hepatocytes in embryonic liver scRNA-seq and endoderm in the mouse gastrulation scRNA-seq data using the *FindConservedMarkers* function in Seurat (v3.1) with Bonferroni-corrected FDR-adjusted P values. Markers were submitted for gene set enrichment ranking and analysis using the Enrichr tool as implemented in the *GSEAPy* (v1.0) package to query the Gene Ontology (GO) Biological Process database (GO_BP_2022) (data S26). Using the *enrichR* package (v3.0) in R, enrichment was first computed by Fisher exact test for randomly sampled genes to derive a mean rank and standard deviation to estimate background for each ontological term accessed. A z -score for deviation of each term to its background rank was then used to rank output genesets. We derived statistical significance (Fisher exact test < 0.05 , ranked by z -score) for each gene set enrichment and performed Markov clustering (MCL) using the MCL (v1.0) package in R to derive network neighborhoods based on geneset intersect. Gene set clusters were annotated using the AutoAnnotate function in the RCy3 (v2.16) package and clusters were ranked by the mean z -score of all gene sets within each cluster and manually curated based on biological relevance. We used the Cytoscape software (v3.9.1) to visualize clusters.

Cell state predictions using probabilistic low-dimensional ElasticNet regression

Label transfer class assignments and median probability of class correspondence between gene expression matrices in single-cell datasets were carried out using a LR framework, as previously described (34), using a similar workflow to the *CellTypist* tool (68).

Raw scRNA-seq datasets being compared were first concatenated, normalized, and log-transformed, as described in preprocessing. HVG selection was performed ($\min_mean = 0.001$, $\max_mean = 10$) for embeddings by dispersion. HVG expression matrices were used as training inputs for models unless otherwise

stated. For models trained in combined low-dimensional representations, linear VAE latent representations were computed using the *LDVAE* module within *scvi-tools* (hidden layers = 256, dropout-rate = 0.2, reconstruction-loss = negative binomial) with donor, dataset origin, and organ information taken as technical covariates. Where PCs were used as input for training, harmony batch-corrected PCs ($k = 100$ pcs) were used, using Harmony (v0.0.9) with technical covariates as described above. Harmony runs were iterated through $\theta = 1:20$ and resultant embeddings benchmarked using kBET and silhouette scores between technical covariates where a low kBET rejection rate and corresponding high silhouette score denoted the optimal θ parameter.

ElasticNet regression (EN) LR models were built using the *sklearn.linear_model.LogisticRegression* module in the *sklearn* package (v0.22). The models were trained using either gene expression data or SCVI batch-corrected low-dimensional LDVAE representation of the training data with regularization parameters (L1-ratio and alpha) tuned using the *GridSearchCV* function in *sklearn* (v1.1.3). The test grid was designed with five l1_ratio intervals (0, 0.2, 0.4, 0.6, 0.8, 1), five alpha (inverse of regularization strength) intervals (0.2, 0.4, 0.6, 0.8, 1) at five train-test splits and three repeats for cross-validation. The unweighted mean over the weighted mean squared errors (MSEs) of each test fold (the cross-validated MSE) was used to determine the optimal model.

The resultant model was used to predict the probability of correspondence between trained labels and precomputed clusters in the target dataset. To ensure that probabilistic outputs from LR models remained consistent with observed neighborhood graph connectivities, the median LR predicted probability of training label assignment was compared against normalized graph distances between classes computed using the *PAGA* (*tl.paga*) module in *Scanpy* as described in our previous work (10) (fig. S13A). Genes predicted to be significantly discriminatory for each LR model were assessed by significance of impact. Features were ranked in descending manner by impact score ($e^{\text{coefficient}}$ per feature for given intercept). Impact significance ($P < 0.05$) of each gene was computed by the survival function (*sf*) across all gene impact scores (fig. S13B). To further verify the specificity of the TREM2 macrophage gene expression profile, the proportion of DEGs overlapping between the TREM2 macrophage population and other macrophage populations across the 12-organ fetal atlas were computed using a two-sided Wilcoxon rank-sum test as described in the clustering and annotation section (fig. S13, C and D, and data S31).

For dataset comparisons across the 12-organ fetal atlas where predesignated labels already existed in the target dataset, the median probability of training label assignment per pre-

designated class was computed. The resultant LR probabilistic relationship between labels of the 12-organ atlas were visualized as a heatmap (figs. S14 and S15 and data S8 to S16).

For classification tasks, a model-specific decision threshold of 0.9 was used to determine predicted labels. Clusters were then assigned classes if the majority projected label had a label count distribution of $>[\text{mean} + (1 \times \text{std})]$ of label counts per cluster. Resultant cell state classifications were further manually checked using DEGs. Further assessment of the predicted cluster labels was carried out by computing the adjusted Rand index and mutual information scores from the modules *sklearn.metrics.adjusted_rand_score* and *sklearn.metrics.mutual_info_score* between the original cluster labels and predicted cluster labels in each dataset. This methodology was applied to classify and annotate several external datasets including the scRNA-seq human gastrulation data (14), the human AGM data (12), the human embryonic liver data and human fetal skin data (48), as well as the human YS and liver CITE-seq data (data S6).

An implementation of the EN workflow described above, in conjunction with the SAMap (self-assembling manifold mapping) workflow (v1.0.7) (69), was used to classify and probabilistically compare cell states across the human YS scRNA-seq data and the mouse gastrulation YS data. A gene-gene sequence homology graph weighted by human and mouse sequence similarity was first constructed using the SAMAP tool. Reciprocal BLAST mapping using the *tblastx* tool between the entire mouse and human transcriptomes for significant homology (E value $< 10^{-6}$) was supplied. The resultant SAM object returned $k = 300$ species-stitched PC components for the top 3000 paired genes. These PC components were used to train the cross-species EN model as a classification task described above (data S11).

LR models and weights trained on the YS and integrated fetal atlases are available via our interactive web portal in “sav” format (see Data and materials availability) and will facilitate future use of our YS atlas for label transfer and to rapidly annotate scRNA-seq datasets using the Python package *CellTypist* (v0.1.9) (68).

Differential lineage priming and progenitor cell fate predictions

The CellRank package (v1.5.1) was used to define and rank fate probabilities of terminal state transitions across annotated hematopoietic lineages in the YS and iPSC scRNA-seq datasets. In the YS data, cell clusters broadly annotated to be in the myeloid lineage were first subsetted from the YS data. After refinement, DCs were excluded from this subset. We did not identify any DCs in the <CS14 (pre-AGM) myeloid lineage. Macrophage trajectory inference was then constructed across the myeloid

subset (fig. S8E). Cells were divided by donors aged <CS14 and >CS14 (post-AGM) and trajectory inference recomputed on new embeddings. First-order kinetics matrices were imputed for each dataset using the *pp.moments* function ($n_pcs = 20$, $n_neighbors = 30$) in the scVelo package (v0.2.4). A Cytotrace pseudotime for state transitions across each dataset was then computed to direct graph-edges toward estimated neighborhood regions of increasing differentiation using the Cytotrace kernel provided within the CellRank package. The resultant KNN and Cytotrace pseudotime were used to compute a probability transition matrix with the *compute_transition_matrix* command in Cytotrace. Neighborhoods of cells representing terminal states of differentiation were identified using true Schur matrix eigen decomposition of the transition matrix *compute_schur* ($n_components = 20$, $method = brandts$), followed by the *compute_macrostates* ($n_states = 10$) command in Cytotrace. The resultant terminally differentiated cell states were then manually selected if multiple terminal states were identified per lineage. Fate absorption probabilities were then computed across all cells terminating at each prespecified terminal cellstate neighborhood using the *compute_absorption_probabilities* command in CellRank. Fate probabilities were then presented as a circular plot using the *pl.circular_projection* with embedding proximity to terminal edges of the graph representing the fate-transition probability of a particular cell toward the prespecified terminally differentiation state. HSPC progenitor population density was then computed by KDE of a precomputed UMAP highlighting relative probabilities of HSPC lineage priming (KDE calculated using the *tl.embedding.density* function in Scanpy).

For HSPC lineage priming analyses which included the respective embryonic erythroid and erythroid terminal states, embryonic erythroid states were defined as any erythroid cell with a HBZ module z -score > 0, and erythroid as any erythroid cell with individual module z -score of HBA1, HBA2, HBG1, HBG2, HBD > 0.

pySCENIC for regulon analysis

The pySCENIC package (v0.9.19) was used to identify TFs and their target genes in the YS and iPSC scRNA-seq datasets. The ranking database (hg38 refseq-r80 500bp_up_and_100bp_down_tss.mc9nr.feather), motif annotation database (motifs-v9-nr.hgnc-m0.001-o0.0.tbl) and list of TFs (lambert2018.txt) were used. An adjacency matrix of TFs and their targets was generated. TF activity from the AUCell output was modeled along diffusion pseudotime rankings of each trajectory and used to train a nonlinear Generalized Additive Model (nlGAM) using the pyGAM.LinearGAM model to identify TF modules which significantly changed across each lineage pseudotime. A gridsearch

of between 50 and 200 splines were calculated. Significantly changing TF regulons across pseudotime were classified with a $P < 0.05$ and reported in Fig. 5, D and H, and data S30). Regulon matrix heatmaps were plotted using the *Seaborn* (v0.12.1) package in Python. Regulon scores were variance-scaled and min-max-standardized with a distribution of 0 to 1.

Cell-cell interaction predictions using CellPhoneDB

To assign putative cell-cell interactions within the YS scRNA-seq dataset, we used CellPhoneDB (v2.1.2). Log-transformed, normalized, and scaled gene expression values for all cell states were exported. CellPhoneDB was run using the statistical method using the receptor-ligand database (v2.0.0) with a significance P cutoff of 0.05 (data S28 and S29). Outputs were ranked by log-mean expression for interactions between cell types of interest in each analyses and plotted as a z -scored heatmap to show standard deviations from mean for each receptor-ligand pair.

HiPlex RNAScope

Human YS tissue (8 PCW) was frozen in OCT compound (Tissue-Tek). 12-plex smFISH was performed using the RNAScope HiPlex v2 assay (ACD, Bio-Techne) on three cryosections (10 μ m) per manufacturer's instructions, using the standard pretreatment for freshly frozen samples and permeabilized with Protease III, for 15 min at room temperature. The imaging cycles, primary probes and label fluorophores were: *Cycle1_KLRB1_AlexaFluor488*, *Cycle1_CD1C_Dylight550*, *Cycle1_IL7R_Dylight650*, *Cycle1_SPINK2_AlexaFluor750*, *Cycle2_P2RY12_AlexaFluor488*, *Cycle2_TNFA_Dylight550*, *Cycle2_LGALS3_Dylight650*, *Cycle2_IL33_AlexaFluor750*, *Cycle3_PLVAP_AlexaFluor488*, *Cycle3_SPINK1_Dylight550*, *Cycle3_C1QA_Dylight650*, *Cycle3_ACTA2_AlexaFluor750*, *Cycle4_P2RY12_Opal570*, and *Cycle4_IBA1_Cy5*. Slides were counterstained with DAPI and coverslipped for imaging.

For protein validation, slides were fixed with 4% (w/v) PFA for 60 min at room temperature and then washed and dehydrated in an ethanol gradient (50 to 100%) for 5 min each. Sections were treated with Protease III (ACD, Bio-Techne) for 15 min at room temperature, then washed with PBS before blocking in 10% (v/v) normal donkey serum containing 1% (w/v) Triton X-100 and 0.2% (w/v) gelatin for 60 min at room temperature. Primary antibodies were incubated at 4°C overnight, then washed three times for 20 min each with a wash buffer [0.1% (w/v) Triton X-100 in PBS]. Slides were blocked with HRP Block (ACD, Bio-Techne) for 60 min at room temperature, and washed with ACD Wash Buffer (ACD, Bio-Techne) before addition of secondary antibody and incubation for 60 min at room temperature. Slides were washed three times for 20 min each [0.1% (w/v) Triton X-100 in PBS]. TSA-Opal570 was added for 10 min at room temperature, then washed three times

with ACD Wash Buffer. Slides were counterstained with DAPI and coverslipped for imaging.

Imaging was performed on a custom two-camera spinning disk confocal microscope built around a Crest Optics X-light v3 module by Cairn Research, a scientific equipment manufacturer. The instrument was controlled using the Micro-Manager software (70). All imaging was performed in spinning disk confocal mode with a 40X water immersion objective [numerical aperture (NA) 1.15, 180 nm per pixel] and 1.5- μ m z -step using Prime BSI Express (Teledyne Photometrics) camera.

RNAScope image analysis

Before each imaging experiment, a slide covered in a sparse layer of 0.5- μ m Tetraspek beads was imaged in all channels. The bead images in all channels were then registered against the beads in the DAPI channel, and their respective affine transforms were saved.

After imaging, each individual tile was z -projected with a maximum intensity projection, then the channels were transformed using the saved affine transforms. The projected, transformed tiles were saved back to a temporary directory along with a bigstitcher-compatible XML file. The BigStitcher software (71) was then used to stitch the transformed tiles together and the final stitched image exported for further analysis.

All imaging cycles for a given tissue section were registered in two steps. First, we used feature registration algorithm implemented in Python via OpenCV-contrib library (version 4.3.0) (72) to compute an affine transformation of DAPI channel from cycle $r > 1$ (moving image) with respect to DAPI channel from the first cycle $r = 1$ (reference image). Key points were detected using the FAST feature detector, whose surrounding areas were described using the DAISY feature descriptor, and the FLANN-based matcher was used to find correspondences between pairs of key points from reference and moving images and filter out unreliable points. The remaining key points were processed using the RANSAC-based algorithm that aligns them and estimates affine transformation parameters with four degrees of freedom.

For the second registration step, a nonlinear registration algorithm based on Farneback optical-flow available in Python via OpenCV library was used to achieve more accurate registration by warping images locally. Specifically, local warping was computed using the DAPI channel, from cycle $r > 1$ with respect to the corresponding channel of the first round. The computational pipeline implementing these registration steps was optimized so that it could be performed efficiently on large images. The corresponding code for feature registration is available at https://github.com/BayraktarLab/feature_reg, and the code for optical-flow registration is available at https://github.com/BayraktarLab/opt_flow_reg.

Immunohistochemistry

Formalin-fixed, paraffin-embedded blocks of YS 4 to 8 PCW, embryonic liver 7 to 8 PCW, and healthy adult liver were sectioned at 4- μ m thickness onto slides coated with 3-aminopropyltriethoxysilane (APES).

For hematoxylin and eosin staining, slides were dewaxed in xylene and rehydrated through graded ethanol, as previously described (10). Rehydrated slides were incubated for 5 min in Mayer's hematoxylin (Dako, Agilent), rinsed in tap water, and then differentiated for 2 s in acid alcohol before washing in tap water followed by Scott's tap water substitute (Leica Biosystems). Sections were counterstained in triple eosin (Dako, Agilent) for 5 min before being rinsed in tap water; dehydrated through graded ethanol (70 to 99%), and then placed in xylene before mounting with DPX (Dako, Agilent).

For immunohistochemistry (IHC), dewaxing, rehydration, and staining was performed using the Discovery Ultra auto Stainer and kits (Ventana, Roche) following the manufacturer's protocols. Primary and secondary antibodies and their concentrations are listed in data S23. Slides were counterstained with one drop of hematoxylin II (Ventana, Roche) for 8 min, rinsed with Reaction Buffer and one drop of Bluing reagent (Dako, Agilent) added for 4 min. The slide was then rinsed with a Reaction buffer, before being dehydrated by hand through graded ethanol (70 to 99%), placed in xylene and mounted with DPX (Dako, Agilent).

Rabbit polyclonal anti-human alpha-1-feto-protein (AFP; Agilent) staining was performed by NovoPath, Newcastle upon Tyne NHS Trust, using a proprietary method.

For the Martius Scarlet eBlue (MSB) stain, slides were dewaxed in xylene and rehydrated through graded ethanol as previously published (10). Rehydrated slides were placed in Bouin's fixative (Atom Scientific) for 1 hour at 60°C, washed in running water; incubated in Weigert's solution (Atom Scientific) for 10 min and washed in water. Slides were differentiated in 0.9% ethanol for 1 to 2 s before rinsing in tap water followed by Scott's tap water substitute (Leica Biosystems), distilled water and finally 95% ethanol. Slides were then incubated stepwise in Martius yellow (3 min) (Atom Scientific), Brilliant crystal scarlet (6 min) (Atom Scientific), and 50% (v/v) Methyl blue (2 min) (Atom Scientific), washing with distilled water between each stain. Slides were washed in tap water; rapidly dehydrated (2 to 3 min) through graded ethanol (70 to 99%), then placed in xylene before mounting with DPX mountant (Dako, Agilent).

All slides were imaged at 20X magnification on a NanoZoomer S360 (Hamamatsu) digital slide scanner. MSB stained images were deconvolved into respective Martius yellow, crystal scarlet and methyl blue channels using the Colour Deconvolution plugin (v1.8) (Masson

Trichrome) in FIJI with thresholds set using the Otsu method. Pseudocolors for each deconvolved channel were then assigned as in Fig. 2C.

ASGR1 and CD34 immunofluorescence microscopy

YS sections were baked onto slides for 2 hours at 60°C before being dewaxed in xylene and rehydrated through graded ethanol as previously described (10). Slides were washed with distilled water then placed in a pressure cooker with boiling citrate buffer pH 6 [10 mM citric acid (Sigma), 0.05% v/v Tween 20 (Sigma) in deionized (DI) water] for 2 min for antigen retrieval. Slides were then washed for 3 min with distilled water followed by 3 min in PBS (Sigma). Sections were blocked with 20% (v/v) goat serum (R&D Systems) for 45 min at room temperature. Primary antibodies were diluted in blocking solution (data S23), added to the sections and incubated for 1 hour at room temperature. Slides were washed twice for 3 min each in a wash buffer [0.1% (w/v) Triton X (Sigma) in PBS], then twice for 3 min each in PBS. Secondary antibodies (see data S23) were diluted in blocking solution, added to section and incubated for 2 hours at room temperature. The wash step was repeated and then 300 nM DAPI (Sigma) was added. Slides were incubated for 5 min before washing with PBS. Slides were then mounted with ProLong Diamond Antifade (ThermoFisher) and imaged on a Zeiss Axioimager with Zeiss ZEN pro software.

SMA and LYVE1/CD34 immunofluorescence microscopy

PFA-fixed YS was cryoprotected with sucrose 10%, embedded in gelatin-sucrose solution [7.5% x/v gelatin (VWR 24350.262), 10% w/v sucrose (VWR27478.296), in 0.12M PBS], frozen at -50°C, then sectioned at 14 μ m. Slides were stored at -80°C until use, dried for 30 min, then blocked with PBS Gelatin Triton [0.2% w/v gelatin, 0.25% Triton X-100 (Sigma-Aldrich) in PBS] for 1 hour. Primary antibodies were diluted in blocking solution (data S23), added to the sections, and incubated overnight. Slides washed with PBS three times at 10-min intervals. Secondary antibodies were diluted in blocking solution and added to sections to incubate for 2 hours (data S23). Hoechst 33258 (Sigma-Aldrich) was added to the secondary antibody solution. Sections were washed with PBS three times at 10-min intervals, and coverslips were mounted with Mowiol (Calbiochem). Sections were imaged at 20X magnification on Leica DM6000 widefield microscope with MetaMorph software. Brightness and contrast were adjusted, and a scale bar was added with FIJI (73).

Light-sheet fluorescence microscopy

Candidate antibodies were screened by immunofluorescence on cryosections obtained from OCT-embedded specimens as previously described (10, 57). Routine light-sheet immuno-

fluorescence microscopy was then performed on floating whole-mount YSs as previously described, with primary antibody incubation reduced to 10 days and secondary reduced to 2 days, both at 37°C to preserve tissue integrity. Antibody and other reagents including nuclear marker TO-PRO-3 iodide are specified in data S23. YSs were embedded in 1.5% agarose blocks before solvent-based clearing as previously described (57). YS retained its spherical shape throughout the procedure. Imaging was performed as previously described in dibenzyl ether with a Miltenyi Biotec Ultramicroscope Blaze (sCMOS camera 5.5MP controlled by Inspector Pro 7.3.2 acquisition software), which generates light sheets at excitation wavelengths of 488, 561, 640, and 785 nm. Objective lenses of 4X magnification (MI Plan 4X, NA 0.35) and 12X magnification (MI Plan, NA 0.53) were used. Imaris (v9.8, BitPlane) was used for image conversion, processing, and video production. Blender 3.0 was used to edit videos and add text. All raw image data are available on request (A.C. and M.H.).

Statistics and reproducibility

The number of cells from each cell type in each de novo single-cell dataset provided in this manuscript are provided in data S4.

REFERENCES AND NOTES

- C. Ross, T. E. Borowiak, Origin and function of the yolk sac in primate embryogenesis. *Nat. Commun.* **11**, 3760 (2020). doi: [10.1038/s41467-020-17575-w](https://doi.org/10.1038/s41467-020-17575-w); pmid: [32724077](https://pubmed.ncbi.nlm.nih.gov/32724077/)
- T. Cindrova-Davies *et al.*, RNA-seq reveals conservation of function among the yolk sacs of human, mouse, and chicken. *Proc. Natl. Acad. Sci. U.S.A.* **114**, E4753–E4761 (2017). doi: [10.1073/pnas.1702560114](https://doi.org/10.1073/pnas.1702560114); pmid: [28559354](https://pubmed.ncbi.nlm.nih.gov/28559354/)
- T. Yamane, Mouse Yolk Sac Hematopoiesis. *Front. Cell Dev. Biol.* **6**, 80 (2018). doi: [10.3389/fcell.2018.00080](https://doi.org/10.3389/fcell.2018.00080); pmid: [30079337](https://pubmed.ncbi.nlm.nih.gov/30079337/)
- J. Palis, J. Malik, K. E. McGrath, P. D. Kingsley, Primitive erythropoiesis in the mammalian embryo. *Int. J. Dev. Biol.* **54**, 1011–1018 (2010). doi: [10.1387/ijdb.093056jp](https://doi.org/10.1387/ijdb.093056jp); pmid: [20711979](https://pubmed.ncbi.nlm.nih.gov/20711979/)
- G. Canu, C. Ruhrberg, First blood: The endothelial origins of hematopoietic progenitors. *Angiogenesis* **24**, 199–211 (2021). doi: [10.1007/s10456-021-09783-9](https://doi.org/10.1007/s10456-021-09783-9); pmid: [33783643](https://pubmed.ncbi.nlm.nih.gov/33783643/)
- A. L. Medvinsky, N. L. Samoylina, A. M. Müller, E. A. Dzierzak, An early pre-liver intraembryonic source of CFU-S in the developing mouse. *Nature* **364**, 64–67 (1993). doi: [10.1038/364064a0](https://doi.org/10.1038/364064a0); pmid: [8316298](https://pubmed.ncbi.nlm.nih.gov/8316298/)
- M. Tavian, M. F. Lallais, B. Péault, Emergence of intraembryonic hematopoietic precursors in the pre-liver human embryo. *Development* **126**, 793–803 (1999). doi: [10.1242/dev.126.4.793](https://doi.org/10.1242/dev.126.4.793); pmid: [9895326](https://pubmed.ncbi.nlm.nih.gov/9895326/)
- C. Peschle *et al.*, Embryonic—Fetal Hb switch in humans: Studies on erythroid bursts generated by embryonic progenitors from yolk sac and liver. *Proc. Natl. Acad. Sci. U.S.A.* **81**, 2416–2420 (1984). doi: [10.1073/pnas.81.8.2416](https://doi.org/10.1073/pnas.81.8.2416); pmid: [6201856](https://pubmed.ncbi.nlm.nih.gov/6201856/)
- Z. Bian *et al.*, Deciphering human macrophage development at single-cell resolution. *Nature* **582**, 571–576 (2020). doi: [10.1038/s41586-020-2316-7](https://doi.org/10.1038/s41586-020-2316-7); pmid: [32499656](https://pubmed.ncbi.nlm.nih.gov/32499656/)
- D.-M. Popescu *et al.*, Decoding human fetal liver haematopoiesis. *Nature* **574**, 365–371 (2019). doi: [10.1038/s41586-019-1652-y](https://doi.org/10.1038/s41586-019-1652-y); pmid: [31597962](https://pubmed.ncbi.nlm.nih.gov/31597962/)
- A. Ivanovs *et al.*, Highly potent human hematopoietic stem cells first emerge in the intraembryonic aorta-gonad-mesonephros region. *J. Exp. Med.* **208**, 2417–2427 (2011). doi: [10.1084/jem.20111688](https://doi.org/10.1084/jem.20111688); pmid: [22042975](https://pubmed.ncbi.nlm.nih.gov/22042975/)
- V. Calvanese *et al.*, Mapping human haematopoietic stem cells from haemogenic endothelium to birth. *Nature* **604**, 534–540 (2022). doi: [10.1038/s41586-022-04571-x](https://doi.org/10.1038/s41586-022-04571-x); pmid: [35418685](https://pubmed.ncbi.nlm.nih.gov/35418685/)

13. D. Horsfall, J. McGrath, Adifa software for Single Cell Insights, v0.1.0, Zenodo (2022); <https://doi.org/10.5281/zenodo.5824896>.
14. R. C. V. Tyser *et al.*, Single-cell transcriptomic characterization of a gastrulating human embryo. *Nature* **600**, 285–289 (2021). doi: [10.1038/s41586-021-04158-y](https://doi.org/10.1038/s41586-021-04158-y); pmid: [34789876](https://pubmed.ncbi.nlm.nih.gov/34789876/)
15. J. Xue *et al.*, Incomplete embryonic lethality and fatal neonatal hemorrhage caused by prothrombin deficiency in mice. *Proc. Natl. Acad. Sci. U.S.A.* **95**, 7603–7607 (1998). doi: [10.1073/pnas.95.13.7603](https://doi.org/10.1073/pnas.95.13.7603); pmid: [9636196](https://pubmed.ncbi.nlm.nih.gov/9636196/)
16. W. Ruf, N. Yokota, F. Schaffner, Tissue factor in cancer progression and angiogenesis. *Thromb. Res.* **125**, S36–S38 (2010). doi: [10.1016/S0049-3848\(10\)70010-4](https://doi.org/10.1016/S0049-3848(10)70010-4); pmid: [20434002](https://pubmed.ncbi.nlm.nih.gov/20434002/)
17. H. Wu, X. Liu, R. Jaenisch, H. F. Lodish, Generation of committed erythroid BFU-E and CFU-E progenitors does not require erythropoietin or the erythropoietin receptor. *Cell* **83**, 59–67 (1995). doi: [10.1016/0092-8674\(95\)90234-1](https://doi.org/10.1016/0092-8674(95)90234-1); pmid: [7553874](https://pubmed.ncbi.nlm.nih.gov/7553874/)
18. I. Hirano, N. Suzuki, The Neural Crest as the First Production Site of the Erythroid Growth Factor Erythropoietin. *Front. Cell Dev. Biol.* **7**, 105 (2019). doi: [10.3389/fcell.2019.00105](https://doi.org/10.3389/fcell.2019.00105); pmid: [31245372](https://pubmed.ncbi.nlm.nih.gov/31245372/)
19. Y. Zhu *et al.*, Characterization and generation of human definitive multipotent hematopoietic stem/progenitor cells. *Cell Discov.* **6**, 89 (2020). doi: [10.1038/s41421-020-00213-6](https://doi.org/10.1038/s41421-020-00213-6); pmid: [33298886](https://pubmed.ncbi.nlm.nih.gov/33298886/)
20. C. Alsinet *et al.*, Robust temporal map of human in vitro myelopoiesis using single-cell genomics. *Nat. Commun.* **13**, 2885 (2022). doi: [10.1038/s41467-022-30557-4](https://doi.org/10.1038/s41467-022-30557-4); pmid: [35610203](https://pubmed.ncbi.nlm.nih.gov/35610203/)
21. C. Peschle *et al.*, Haemoglobin switching in human embryos: Asynchrony of $\zeta \rightarrow \alpha$ and $\epsilon \rightarrow \gamma$ -globin switches in primitive and definitive erythropoietic lineage. *Nature* **313**, 235–238 (1985). doi: [10.1038/313235a0](https://doi.org/10.1038/313235a0); pmid: [2578614](https://pubmed.ncbi.nlm.nih.gov/2578614/)
22. J. Palis, Primitive and definitive erythropoiesis in mammals. *Front. Physiol.* **5**, 3 (2014). doi: [10.3389/fphys.2014.00003](https://doi.org/10.3389/fphys.2014.00003); pmid: [24478716](https://pubmed.ncbi.nlm.nih.gov/24478716/)
23. W. Liu *et al.*, Trem2 promotes anti-inflammatory responses in microglia and is suppressed under pro-inflammatory conditions. *Hum. Mol. Genet.* **29**, 3224–3248 (2020). doi: [10.1093/hmg/ddaa209](https://doi.org/10.1093/hmg/ddaa209); pmid: [32959884](https://pubmed.ncbi.nlm.nih.gov/32959884/)
24. D. A. Jaitin *et al.*, Lipid-Associated Macrophages Control Metabolic Homeostasis in a Trem2-Dependent Manner. *Cell* **178**, 686–698.e14 (2019). doi: [10.1016/j.cell.2019.05.054](https://doi.org/10.1016/j.cell.2019.05.054); pmid: [31257031](https://pubmed.ncbi.nlm.nih.gov/31257031/)
25. Y. Wang *et al.*, TREM2 lipid sensing sustains the microglial response in an Alzheimer's disease model. *Cell* **160**, 1061–1071 (2015). doi: [10.1016/j.cell.2015.01.049](https://doi.org/10.1016/j.cell.2015.01.049); pmid: [25728668](https://pubmed.ncbi.nlm.nih.gov/25728668/)
26. T. Jaffredo, R. Gautier, A. Eichmann, F. Dieterlen-Lièvre, Intra-aortic hematopoietic cells are derived from endothelial cells during ontogeny. *Development* **125**, 4575–4583 (1998). doi: [10.1242/dev.125.22.4575](https://doi.org/10.1242/dev.125.22.4575); pmid: [9778515](https://pubmed.ncbi.nlm.nih.gov/9778515/)
27. L. Yvernogeu *et al.*, In vivo generation of haematopoietic stem/progenitor cells from bone marrow-derived haemogenic endothelium. *Nat. Cell Biol.* **21**, 1334–1345 (2019). doi: [10.1038/s41556-019-0410-6](https://doi.org/10.1038/s41556-019-0410-6); pmid: [31685991](https://pubmed.ncbi.nlm.nih.gov/31685991/)
28. Z. Li *et al.*, Mouse embryonic head as a site for hematopoietic stem cell development. *Cell Stem Cell* **11**, 663–675 (2012). doi: [10.1016/j.stem.2012.07.004](https://doi.org/10.1016/j.stem.2012.07.004); pmid: [23122290](https://pubmed.ncbi.nlm.nih.gov/23122290/)
29. J. M. Frame, K. H. Fegan, S. J. Conway, K. E. McGrath, J. Palis, Definitive Hematopoiesis in the Yolk Sac Emerges from Wnt-Responsive Hemogenic Endothelium Independently of Circulation and Arterial Identity. *Stem Cells* **34**, 431–444 (2016). doi: [10.1002/stem.2213](https://doi.org/10.1002/stem.2213); pmid: [26418893](https://pubmed.ncbi.nlm.nih.gov/26418893/)
30. K. E. Rhodes *et al.*, The emergence of hematopoietic stem cells is initiated in the placental vasculature in the absence of circulation. *Cell Stem Cell* **2**, 252–263 (2008). doi: [10.1016/j.stem.2008.01.001](https://doi.org/10.1016/j.stem.2008.01.001); pmid: [18371450](https://pubmed.ncbi.nlm.nih.gov/18371450/)
31. Y. Zeng *et al.*, Tracing the first hematopoietic stem cell generation in human embryo by single-cell RNA sequencing. *Cell Res.* **29**, 881–894 (2019). doi: [10.1038/s41422-019-0228-6](https://doi.org/10.1038/s41422-019-0228-6); pmid: [31501518](https://pubmed.ncbi.nlm.nih.gov/31501518/)
32. R. Thambyrajah *et al.*, GFIL proteins orchestrate the emergence of hematopoietic stem cells through recruitment of LSD1. *Nat. Cell Biol.* **18**, 21–32 (2016). doi: [10.1038/ncb3276](https://doi.org/10.1038/ncb3276); pmid: [26619147](https://pubmed.ncbi.nlm.nih.gov/26619147/)
33. M. Efremova, M. Vento-Tormo, S. A. Teichmann, R. Vento-Tormo, CellPhoneDB: inferring cell–cell communication from combined expression of multi-subunit ligand–receptor complexes. *Nat. Protoc.* **15**, 1484–1506 (2020). doi: [10.1038/s41596-020-0292-x](https://doi.org/10.1038/s41596-020-0292-x); pmid: [32103204](https://pubmed.ncbi.nlm.nih.gov/32103204/)
34. L. Jardine *et al.*, Blood and immune development in human fetal bone marrow and Down syndrome. *Nature* **598**, 327–331 (2021). doi: [10.1038/s41586-021-03929-x](https://doi.org/10.1038/s41586-021-03929-x); pmid: [34588693](https://pubmed.ncbi.nlm.nih.gov/34588693/)
35. J. Fröbel *et al.*, The Hematopoietic Bone Marrow Niche Ecosystem. *Front. Cell Dev. Biol.* **9**, 705410 (2021). doi: [10.3389/fcell.2021.705410](https://doi.org/10.3389/fcell.2021.705410); pmid: [34368155](https://pubmed.ncbi.nlm.nih.gov/34368155/)
36. B. Murdoch *et al.*, Wnt-5A augments repopulating capacity and primitive hematopoietic development of human blood stem cells in vivo. *Proc. Natl. Acad. Sci. U.S.A.* **100**, 3422–3427 (2003). doi: [10.1073/pnas.0130233100](https://doi.org/10.1073/pnas.0130233100); pmid: [12626754](https://pubmed.ncbi.nlm.nih.gov/12626754/)
37. J. Shen *et al.*, Vitronectin-activated $\alpha v \beta 3$ and $\alpha v \beta 5$ integrin signalling specifies haematopoietic fate in human pluripotent stem cells. *Cell Prolif.* **54**, e13012 (2021). doi: [10.1111/cpr.13012](https://doi.org/10.1111/cpr.13012); pmid: [33656760](https://pubmed.ncbi.nlm.nih.gov/33656760/)
38. P. Zhang *et al.*, The physical microenvironment of hematopoietic stem cells and its emerging roles in engineering applications. *Stem Cell Res. Ther.* **10**, 327 (2019). doi: [10.1186/s13287-019-1422-7](https://doi.org/10.1186/s13287-019-1422-7); pmid: [31744536](https://pubmed.ncbi.nlm.nih.gov/31744536/)
39. A. S. Eisele *et al.*, Erythropoietin directly remodels the clonal composition of murine hematopoietic multipotent progenitor cells. *eLife* **11**, e66922 (2022). doi: [10.7554/eLife.66922](https://doi.org/10.7554/eLife.66922); pmid: [35166672](https://pubmed.ncbi.nlm.nih.gov/35166672/)
40. H. Yoshihara *et al.*, Thrombopoietin/MPL signaling regulates hematopoietic stem cell quiescence and interaction with the osteoblastic niche. *Cell Stem Cell* **1**, 685–697 (2007). doi: [10.1016/j.stem.2007.10.020](https://doi.org/10.1016/j.stem.2007.10.020); pmid: [18371409](https://pubmed.ncbi.nlm.nih.gov/18371409/)
41. F. Ginhoux, M. Guilliams, Tissue-Resident Macrophage Ontogeny and Homeostasis. *Immunity* **44**, 439–449 (2016). doi: [10.1016/j.immuni.2016.02.024](https://doi.org/10.1016/j.immuni.2016.02.024); pmid: [26982352](https://pubmed.ncbi.nlm.nih.gov/26982352/)
42. C. Gekas *et al.*, Mef2C is a lineage-restricted target of Scf/Tal1 and regulates megakaryopoiesis and B-cell homeostasis. *Blood* **113**, 3461–3471 (2009). doi: [10.1182/blood-2008-07-167577](https://doi.org/10.1182/blood-2008-07-167577); pmid: [19211936](https://pubmed.ncbi.nlm.nih.gov/19211936/)
43. E. Suzuki *et al.*, The transcription factor Fli-1 regulates monocyte, macrophage and dendritic cell development in mice. *Immunology* **139**, 318–327 (2013). doi: [10.1111/imm.12070](https://doi.org/10.1111/imm.12070); pmid: [23320737](https://pubmed.ncbi.nlm.nih.gov/23320737/)
44. M. L. Petreaca, M. Yao, Y. Liu, K. Defea, M. Martins-Green, Transactivation of vascular endothelial growth factor receptor-2 by interleukin-8 (IL-8/CXCL8) is required for IL-8/CXCL8-induced endothelial permeability. *Mol. Biol. Cell* **18**, 5014–5023 (2007). doi: [10.1091/mbc.e07-01-0004](https://doi.org/10.1091/mbc.e07-01-0004); pmid: [17928406](https://pubmed.ncbi.nlm.nih.gov/17928406/)
45. Z. Lyu *et al.*, Effects of NRPI on angiogenesis and vascular maturity in endothelial cells are dependent on the expression of SEMA4D. *Int. J. Mol. Med.* **46**, 1321–1334 (2020). doi: [10.3892/ijmm.2020.4692](https://doi.org/10.3892/ijmm.2020.4692); pmid: [32945351](https://pubmed.ncbi.nlm.nih.gov/32945351/)
46. K. Bisht *et al.*, Capillary-associated microglia regulate vascular structure and function through PANX1-P2RY12 coupling in mice. *Nat. Commun.* **12**, 5289 (2021). doi: [10.1038/s41467-021-25590-8](https://doi.org/10.1038/s41467-021-25590-8); pmid: [34489419](https://pubmed.ncbi.nlm.nih.gov/34489419/)
47. F. Ginhoux *et al.*, Fate mapping analysis reveals that adult microglia derive from primitive macrophages. *Science* **330**, 841–845 (2010). doi: [10.1126/science.1194637](https://doi.org/10.1126/science.1194637); pmid: [20966214](https://pubmed.ncbi.nlm.nih.gov/20966214/)
48. C. Suo *et al.*, Mapping the developing human immune system across organs. *Science* **376**, eabo0510 (2022). doi: [10.1126/science.abo0510](https://doi.org/10.1126/science.abo0510); pmid: [35549310](https://pubmed.ncbi.nlm.nih.gov/35549310/)
49. L. Garcia-Alonso *et al.*, Single-cell roadmap of human gonadal development. *Nature* **607**, 540–547 (2022). doi: [10.1038/s41586-022-04918-4](https://doi.org/10.1038/s41586-022-04918-4); pmid: [35794482](https://pubmed.ncbi.nlm.nih.gov/35794482/)
50. S. A. Dick *et al.*, Three tissue resident macrophage subsets coexist across organs with conserved origins and life cycles. *Sci. Immunol.* **7**, eab7777 (2022). doi: [10.1126/sciimmunol.ab7777](https://doi.org/10.1126/sciimmunol.ab7777); pmid: [34995099](https://pubmed.ncbi.nlm.nih.gov/34995099/)
51. A. Gayoso *et al.*, A Python library for probabilistic analysis of single-cell omics data. *Nat. Biotechnol.* **40**, 163–166 (2022). doi: [10.1038/s41587-021-01206-w](https://doi.org/10.1038/s41587-021-01206-w); pmid: [35132262](https://pubmed.ncbi.nlm.nih.gov/35132262/)
52. R. Lopez, J. Regier, M. B. Cole, M. I. Jordan, N. Yosef, Deep generative modeling for single-cell transcriptomics. *Nat. Methods* **15**, 1053–1058 (2018). doi: [10.1038/s41587-018-0229-2](https://doi.org/10.1038/s41587-018-0229-2); pmid: [30504886](https://pubmed.ncbi.nlm.nih.gov/30504886/)
53. S. Chou, H. F. Lodish, Fetal liver hepatic progenitors are supportive stromal cells for hematopoietic stem cells. *Proc. Natl. Acad. Sci. U.S.A.* **107**, 7799–7804 (2010). doi: [10.1073/pnas.1003586107](https://doi.org/10.1073/pnas.1003586107); pmid: [20385801](https://pubmed.ncbi.nlm.nih.gov/20385801/)
54. M.-L. N. Ton *et al.*, Rabbit Development as a Model for Single Cell Comparative Genomics. *bioRxiv* 2022.10.06.510971 [Preprint] (2022). <https://doi.org/10.1101/2022.10.06.510971>
55. U. C. Eze, A. Bhaduri, M. Haeussler, T. J. Nowakowski, A. R. Kriegstein, Single-cell atlas of early human brain development highlights heterogeneity of human neuroepithelial cells and early radial glia. *Nat. Neurosci.* **24**, 584–594 (2021). doi: [10.1038/s41593-020-00794-1](https://doi.org/10.1038/s41593-020-00794-1); pmid: [33723434](https://pubmed.ncbi.nlm.nih.gov/33723434/)
56. T. Strachan, S. Lindsay, D. I. Wilson, *Molecular Genetics of Early Human Development* (Academic Press, 1997).
57. M. Belle *et al.*, Tridimensional Visualization and Analysis of Early Human Development. *Cell* **169**, 161–173.e12 (2017). doi: [10.1016/j.cell.2017.03.008](https://doi.org/10.1016/j.cell.2017.03.008); pmid: [28340341](https://pubmed.ncbi.nlm.nih.gov/28340341/)
58. A.-C. Villani *et al.*, Single-cell RNA-seq reveals new types of human blood dendritic cells, monocytes, and progenitors. *Science* **356**, eaah4573 (2017). doi: [10.1126/science.aah4573](https://doi.org/10.1126/science.aah4573); pmid: [28428369](https://pubmed.ncbi.nlm.nih.gov/28428369/)
59. S. L. Wolock, R. Lopez, A. M. Klein, Scrublet: Computational Identification of Cell Doubts in Single-Cell Transcriptomic Data. *Cell Syst.* **8**, 281–291.e9 (2019). doi: [10.1016/j.cels.2018.11.005](https://doi.org/10.1016/j.cels.2018.11.005); pmid: [30954476](https://pubmed.ncbi.nlm.nih.gov/30954476/)
60. S. J. Fleming *et al.*, Unsupervised removal of systematic background noise from droplet-based single-cell experiments using CellBender. *bioRxiv* 791699 [Preprint] (2022). <https://doi.org/10.1101/791699>
61. F. A. Wolf, P. Angerer, F. J. Theis, SCANPY: Large-scale single-cell gene expression data analysis. *Genome Biol.* **19**, 15 (2018). doi: [10.1186/s13059-017-1382-0](https://doi.org/10.1186/s13059-017-1382-0); pmid: [29409532](https://pubmed.ncbi.nlm.nih.gov/29409532/)
62. M. P. Mülé, A. J. Martins, J. S. Tsang, Normalizing and denoising protein expression data from droplet-based single cell profiling. *Nat. Commun.* **13**, 2099 (2022). doi: [10.1038/s41467-022-29356-8](https://doi.org/10.1038/s41467-022-29356-8); pmid: [35440536](https://pubmed.ncbi.nlm.nih.gov/35440536/)
63. H. Wang *et al.*, Decoding Human Megakaryocyte Development. *Cell Stem Cell* **28**, 535–549.e8 (2021). doi: [10.1016/j.stem.2020.11.006](https://doi.org/10.1016/j.stem.2020.11.006); pmid: [33340451](https://pubmed.ncbi.nlm.nih.gov/33340451/)
64. I. Korsunsky *et al.*, Fast, sensitive and accurate integration of single-cell data with Harmony. *Nat. Methods* **16**, 1289–1296 (2019). doi: [10.1038/s41592-019-0619-0](https://doi.org/10.1038/s41592-019-0619-0); pmid: [31740819](https://pubmed.ncbi.nlm.nih.gov/31740819/)
65. M. Büttner, Z. Miao, F. A. Wolf, S. A. Teichmann, F. J. Theis, A test metric for assessing single-cell RNA-seq batch correction. *Nat. Methods* **16**, 43–49 (2019). doi: [10.1038/s41592-018-0254-1](https://doi.org/10.1038/s41592-018-0254-1); pmid: [30573817](https://pubmed.ncbi.nlm.nih.gov/30573817/)
66. V. A. Traag, L. Waltman, N. J. van Eck, From Louvain to Leiden: Guaranteeing well-connected communities. *Sci. Rep.* **9**, 5233 (2019). doi: [10.1038/s41598-019-41695-z](https://doi.org/10.1038/s41598-019-41695-z); pmid: [30914743](https://pubmed.ncbi.nlm.nih.gov/30914743/)
67. E. Dann, N. C. Henderson, S. A. Teichmann, M. D. Morgan, J. C. Marioni, Differential abundance testing on single-cell data using k-nearest neighbor graphs. *Nat. Biotechnol.* **40**, 245–253 (2022). doi: [10.1038/s41587-021-01033-z](https://doi.org/10.1038/s41587-021-01033-z); pmid: [34594043](https://pubmed.ncbi.nlm.nih.gov/34594043/)
68. C. Domínguez Conde *et al.*, Cross-tissue immune cell analysis reveals tissue-specific features in humans. *Science* **376**, eab5197 (2022). doi: [10.1126/science.ab5197](https://doi.org/10.1126/science.ab5197); pmid: [35549406](https://pubmed.ncbi.nlm.nih.gov/35549406/)
69. A. J. Tarashansky *et al.*, Mapping single-cell atlases throughout Metazoa unravels cell type evolution. *eLife* **10**, e66747 (2021). doi: [10.7554/eLife.66747](https://doi.org/10.7554/eLife.66747); pmid: [33944782](https://pubmed.ncbi.nlm.nih.gov/33944782/)
70. A. Edelstein, N. Amodaj, K. Hoover, R. Vale, N. Stuurman, Computer control of microscopes using uManager. *Curr. Protoc. Mol. Biol.* **92**, 14.20.1–14.20.17 (2010). doi: [10.1002/0471142727.mbl420592](https://doi.org/10.1002/0471142727.mbl420592); pmid: [20890901](https://pubmed.ncbi.nlm.nih.gov/20890901/)
71. D. Hori *et al.*, BigStitcher: Reconstructing high-resolution image datasets of cleared and expanded samples. *Nat. Methods* **16**, 870–874 (2019). doi: [10.1038/s41592-019-0501-0](https://doi.org/10.1038/s41592-019-0501-0); pmid: [31384047](https://pubmed.ncbi.nlm.nih.gov/31384047/)
72. M. Gataric *et al.*, PoStcode: Probabilistic image-based spatial transcriptomics decoder. *bioRxiv* 2021.10.12.464086 [Preprint] (2021). <https://doi.org/10.1101/2021.10.12.464086>
73. J. Schindelin *et al.*, Fiji: An open-source platform for biological-image analysis. *Nat. Methods* **9**, 676–682 (2012). doi: [10.1038/nmeth.2019](https://doi.org/10.1038/nmeth.2019); pmid: [22743772](https://pubmed.ncbi.nlm.nih.gov/22743772/)
74. B. J. Stewart *et al.*, Spatiotemporal immune zonation of the human kidney. *Science* **365**, 1461–1466 (2019). doi: [10.1126/science.aab5031](https://doi.org/10.1126/science.aab5031); pmid: [31604275](https://pubmed.ncbi.nlm.nih.gov/31604275/)
75. I. Imaz-Rosshandler *et al.*, “Tracking Early Mammalian Organogenesis – Prediction and Validation of Differentiation Trajectories at Whole Organism Scale,” (2023); <https://marionilab.github.io/ExtendedMouseAtlas/>.
76. E. I. Crosse *et al.*, Multi-layered Spatial Transcriptomics Identify Secretory Factors Promoting Human Hematopoietic Stem Cell Development. *Cell Stem Cell* **27**, 822–839.e8 (2020). doi: [10.1016/j.stem.2020.08.004](https://doi.org/10.1016/j.stem.2020.08.004); pmid: [32946788](https://pubmed.ncbi.nlm.nih.gov/32946788/)
77. M. Mather, M. Haniffa, R. Botting, S. Webb, “The role of the yolk sac in human fetal development and identification of a hepatocyte-like cell in the human yolk sac,” BioStudies, E-MTAB-10552 (2023); <https://www.ebi.ac.uk/biostudies/arrayexpress/studies/E-MTAB-10552>.
78. S. Webb, M. Haniffa, E. Stephenson, “Human fetal yolk sac scRNA-seq data (sample ID: F158 for Haniffa Lab; 16099 for HDBR),” BioStudies, E-MTAB-11673 (2022); <https://www.ebi.ac.uk/biostudies/arrayexpress/studies/E-MTAB-11673>.
79. M. Haniffa, M. Mather, R. Botting, “The role of the yolk sac in human fetal development and identification of a hepatocyte-like cell in the human yolk sac (SS2),” BioStudies, E-MTAB-10888 (2023); <https://www.ebi.ac.uk/biostudies/arrayexpress/studies/E-MTAB-10888>.
80. M. Haniffa, E. Stephenson, S. Webb, “Human embryonic yolk sac CITE-seq data,” BioStudies, E-MTAB-11549 (2022);

<https://www.ebi.ac.uk/biostudies/arrayexpress/studies/E-MTAB-11549>.

81. S. Webb, E. Stephenson, M. Haniffa, "Human embryonic liver CITE-seq data," BioStudies, E-MTAB-11618 (2022); <https://www.ebi.ac.uk/biostudies/arrayexpress/studies/E-MTAB-11618>.
82. E. Stephenson, S. Webb, M. Haniffa, "Human fetal liver CITE-seq data," BioStudies, E-MTAB-11613 (2022); <https://www.ebi.ac.uk/biostudies/arrayexpress/studies/E-MTAB-11613>.
83. I. Goh, FCA_yolkSac, v1.0.0, Zenodo (2023); <https://doi.org/10.5281/zenodo.7868304>.
84. I. Goh, M. Inoue, R. Botting, M. Haniffa, "Yolk sac cell atlas reveals multiorgan functions during early development," BioStudies, S-DHCA0 (2022); <https://www.ebi.ac.uk/biostudies/bioimages/studies/S-DHCA0>.

ACKNOWLEDGMENTS

We thank T. Dhanaseelan of HDBR for assistance with human fetal tissue processing and cell freezing, N. Elliott for contributions toward CITE-seq panel design, S. Fouquet and Q. Rappeneau for technical support, and J. Haniffa for copyediting support. We also thank the Newcastle University Flow Cytometry Core Facility, Newcastle University Genomics Facility, Sanger Institute Cellular Genetics IT, CRUK CI Genomics Core Facility, and Newcastle upon Tyne NHS Trust NovoPath. We are grateful to the donors and donor families for granting access to the tissue samples. This publication is part of the Human Cell Atlas (www.humancellatlas.org/publications). **Funding:** We acknowledge funding from the Wellcome Human Cell Atlas Strategic Science Support (WT211276/Z/18/Z), an MRC Human Cell Atlas award, the Wellcome Human Developmental Biology Initiative (WT215116/Z/18/Z), and HDBR (MRC/Wellcome MR/R006237/1). M.H. is funded by Wellcome (WT107931/Z/15/Z, WT223092/Z/21/Z, WT206194, and WT220540/Z/20/A), the Lister Institute for Preventive Medicine, and NIHR and Newcastle Biomedical Research Centre. S.A.T. is funded by Wellcome (WT206194) and the ERC Consolidator Grant ThDEFINE. Relevant research in the B.G. group was funded by Wellcome (206328/Z/17/Z) and the MRC (MR/

MO08975/1 and MR/S036113/1). I.R. is funded by Blood Cancer UK and by the NIHR Oxford Biomedical Centre Research Fund. E.L. is funded by a Sir Henry Dale Fellowship jointly funded by the Wellcome Trust and the Royal Society (107630/Z/15/A). L.J. is funded by a Newcastle Health Innovation Partners Lectureship. M.Ma. is funded by an Action Medical Research Fellowship (GN2779). N.M. was funded by a DFG Research Fellowship (ME 5209/1-1). S.Be. is funded by a Wellcome Senior Research Fellowship (10104/Z/15/Z). C.AI. is funded by the Open Targets consortium (OTAR026 project) and Wellcome Sanger core funding (WT206194). M.I. is supported by Wellcome (215116/Z/18/Z) and thanks the PhD program FIRE and the Graduate School EURIP of Université Paris Cité for their financial support. J.Pal. is funded by NIH NHLBI R01 (HL151777). J.T.H.L. is funded by the Wellcome Trust Grant (108413/A/15/D). A.C. is funded by the Inserm cross-cutting program HuDeCA 2018. M.d.B. is funded by an MRC Molecular Haematology Unit core award MC_UU_00029/5. B.O. is funded by a Wellcome 4Ward North Clinical Training Fellowship.

Author contributions: Conceptualization: M.H., S.A.T., and B.G. Funding acquisition: M.H., S.A.T., and B.G. Supervision: M.H. and L.J. Data curation: I.G., A.R., S.W., M.Ma., M.Q.L., N.K.W., D.H., and D.B.L. Formal analysis: I.G., A.R., K.G., S.W., I.I.-R., M.Q.L., D.-M.P., K.P., J.Par., S.v.D., J.T.H.L., M.-L.T., D.K., L.Y., and N.K.W. Software: D.H. and D.B.-L. Investigation: R.A.B., S.L., D.J.H., J.E., E.S., I.G., N.K.W., N.-J.C., N.M., R.H., M.S.V., Y.G., M.I., D.D., M.A., R.C., T.N., K.K., E.T., S.J.K., and V.L. Methodology: R.A.B., E.S., O.B., K.K., N.-J.C., V.R., M.I., and Y.G. Resources: C.AI., R.V.-T., S.Ba., P.M., L.G., K.B.M., S.Be., E.L., A.C., I.R., M.d.B., E.D., C.S., and J.M. Writing – original draft: L.J., S.W., I.G., M.H., R.A.B., B.O., M.Mi., and E.S. Writing – review & editing: L.J., I.G., S.W., E.S., M.H., A.R., J.E., R.A.B., B.G., M.Mi., and J.Pal. Visualization: J.E., R.A.B., L.J., C.Ad., I.G., A.R., M.-L.T., and S.W. **Competing interests:** J.M. is an employee of Genentech. The remaining authors declare no competing interests. **Data and materials availability:** All raw sequencing data from this study are made publicly available at ArrayExpress as FASTQs and count matrices as follows: (i) human EL and YS 10X scRNA-seq (77), (ii) human embryonic YS 10X

scRNA-seq (78), (iii) human embryonic YS Smart-seq2 scRNA-seq (79), (iv) human embryonic YS CITE-seq (80), (v) human EL CITE-seq (81), and (vi) human fetal liver CITE-seq (82). Accessions for published data reused in this study are detailed comprehensively in data S6. Processed single-cell datasets are available for interactive exploration and download as well as corresponding trained scVI and LR models via our interactive web portal (<https://developmental.cellatlas.io/yolk-sac>). Note, data on portals are best used for rapid visualization. For formal analysis and all code for reproducibility, including trained scVI VAE, IdVAE, and trained LR models, we recommended following our archived code available on Github (83) and our interactive web portal. All raw and processed imaging data are available on the EBI BioImage Archive (84). Processed imaging data are available on our interactive web portal. **License information:** Copyright © 2023 the authors, some rights reserved; exclusive licensee American Association for the Advancement of Science. No claim to original US government works. <https://www.science.org/about/science-licenses-journal-article-reuse>. This research was funded in whole or in part by Wellcome (WT211276/Z/18/Z, MR/R006237/1, WT107931/Z/15/Z, WT223092/Z/21/Z, WT206194, WT220540/Z/20/A, WT206194, 206328/Z/17/Z, 107630/Z/15/A, 10104/Z/15/Z, WT206194, 215116/Z/18/Z, and 108413/A/15/D), a cOAllition S organization. The author will make the Author Accepted Manuscript (AAM) version available under a CC BY public copyright license.

SUPPLEMENTARY MATERIALS

science.org/doi/10.1126/science.add7564

Figs. S1 to S15

References (85–88)

MDAR Reproducibility Checklist

Movies S1 and S2

Data S1 to S33

Submitted 4 July 2022; resubmitted 6 December 2022

Accepted 3 July 2023

10.1126/science.add7564